RESEARCH ARTICLE

Are Finite-Amplitude Effects Important in Non-Breaking Mountain Waves?

Johnathan J. Metz[1] | **Dale R. Durran**[1]

[1]Department of Atmospheric Sciences, University of Washington, Seattle, WA, 98195, USA

Correspondence
408 Atmospheric Sciences-Geophysics (ATG) Building, Box 351640, Seattle, WA, 98115, USA
Email: jjmetz@uw.edu

Funding information
U.S. National Science Foundation, Grant Number: AGS-1929466

Linear theory has long been used to study mountain waves and has been successful in describing much of their behaviour. In the simplest theoretical context, that of two-dimensional steady-state flow with constant Brunt-Väisälä frequency (N) and horizontal wind speed (U), finite-amplitude effects are relatively minor until wave breaking occurs. However, in more complex environmental profiles, significant finite-amplitude effects occur below the wave-breaking threshold. We constructed a linearized version of a fully nonlinear time-dependent model, thereby facilitating direct comparisons between linear and finite-amplitude solutions in cases with upstream profiles representative of typical real-world events.

Beginning with the simplest profile that includes a tropopause, namely an environment with constant upstream wind speed and two layers of constant static stability, we progressively investigate more complex profiles that include vertical wind shear typical of the mid-latitude westerlies. Our results demonstrate that even without wave breaking, finite-amplitude effects can play an important role in modulating the mountain-wave amplitude and gravity-wave drag. The modulation is a function of the tropopause height and is most pronounced when the cross-ridge flow increases strongly with height.

KEYWORDS
finite-amplitude, nonlinearity, mountain wave, gravity wave drag

1 | INTRODUCTION AND BACKGROUND

Linear theory has been applied to the study of mountain waves for decades, including some of the earliest works on the subject (Queney, 1948; Scorer, 1949) and some of the latest analysis of observational data (Smith and Kruse, 2017). The relationship derived by Eliassen and Palm (1960) between vertical energy and momentum fluxes for steady nondissipating mountain waves has been verified using observations from recent field campaigns (Smith et al., 2008, 2016). Wentzel-Kramers-Brillouin (WKB) ray-tracing has been successfully used to explain gravity propagation into the middle atmosphere (Marks and Eckermann, 1995; Guest et al., 2000). There is, therefore, considerable evidence that linear theory provides a reasonably good approximation to the dynamics governing gravity-wave propagation through much of the atmosphere.

Partly for this reason, as well as for simplicity and to minimize computational cost, linear theory is widely used in the parameterization of orographic gravity wave drag (GWD) in both numerical weather prediction (NWP) and general circulation models (GCMs). In particular, the estimate of the low-level mountain-wave momentum flux typically uses the functional dependence on the near-surface wind U_s, static stability N_s, and the unblocked mountain height h_{ub} given by linear-theory: $N_s U_s h_{\mathrm{ub}}^2$. Farther aloft, the changes in wave amplitude and the level of wave breaking are parameterized using the WKB assumption (e.g. Palmer et al., 1986; McFarlane, 1987; Kim and Arakawa, 1995; Kim et al., 2003; Kim and Doyle, 2005). While improvements to orographic GWD parameterizations have been made to include low-level flow blocking (e.g. Lott and Miller, 1997; Kim and Doyle, 2005) and mountain anisotropy (e.g. Scinocca and McFarlane, 2000; Kim and Doyle, 2005; Choi and Hong, 2015), major global modelling centres such as the U.S. National Centers for Environmental Prediction (NCEP; Chen et al., 2019; Zhou et al., 2019), the European Centre for Medium-Range Weather Forecasts (ECMWF; Sandu et al., 2016; ECMWF, 2020), and the UK Met Office (Walters et al., 2017) continue to estimate the momentum flux in the waves launched by the mountain as proportional to $N_s U_s h_{\mathrm{ub}}^2$.

Nevertheless, nonlinear processes can be important in setting the amplitude at which mountain waves are generated, but the importance of nonlinearity in regulating wave amplitude is poorly understood, perhaps because so much theoretical attention as been devoted to the special case in which the upstream environmental Brunt-Väisälä frequency $N(z)$ and the cross-mountain wind speed $U(z)$ are constant with height. When N and U are constant, the streamline displacement $\delta(x,z)$ in steady two-dimensional Boussinesq flow over such a ridge is governed by Long's equation (Long, 1953),

$$\left(\frac{\partial^2}{\partial x^2} + \frac{\partial^2}{\partial z^2}\right)\delta + \frac{N^2}{U^2}\delta = 0. \tag{1}$$

Here x is the horizontal coordinate perpendicular to the ridge-line; z is the vertical coordinate.

Although Long's equation is a linear partial differential equation, it may be derived from the fully nonlinear equations without making any small-amplitude assumptions. Nevertheless, if U is constant, Eq. 1 may also be derived by assuming the mountain is infinitesimally high and linearizing the governing equations in the usual manner. When N and U are constant, the only difference between the linear and nonlinear solutions arises from the lower boundary condition. Letting $h(x)$ be the height of the topography, the lower boundary condition requires $\delta\,[x, h(x)] = h(x)$ in the exact finite-amplitude case and is approximated by $\delta(x,0) = h(x)$ in the small-amplitude limit.

As one might guess from the similarities in the governing equations for linear and finite-amplitude perturbations, when N and U are constant the influence of nonlinear dynamics on the wave structure is often relatively minor. This

similarity can be appreciated by comparing the linear and nonlinear solutions[1] in Fig. 1, which is for a case with $N = 0.01\,\mathrm{s}^{-1}$, $U = 10\,\mathrm{m/s}$, and $Nh_m/U = 0.6$, where h_m is the mountain height. Nonlinear processes steepen the streamlines above the mountain around $z = 4.5\,\mathrm{km}$, which is $3/4$ of a hydrostatic vertical wavelength $(2\pi U/N)$ above the topography. Despite the modest differences in the shape of the streamlines between the linear and nonlinear waves, the wave amplitude is almost identical in both cases. Hence, nonlinear processes do not have a dramatic impact on the mountain-wave momentum flux generated in constant-N-and-U flow over a ridge unless the ridge is high enough to force wave overturning.

In contrast to the constant-N idealization, there is typically a factor of two change in static stability between the troposphere and the lower stratosphere, and changes in the height of a sharp tropopause can strongly modulate the strength of momentum fluxes associated with vertically propagating hydrostatic mountain waves. If there is a factor of two difference in N across the tropopause and U is the same constant value in both layers, the ratio of the momentum fluxes in the optimally tuned case to the maximally detuned case is a factor of four in linear mountain waves (Blumen, 1965; Klemp and Lilly, 1975). The wave reflections at the tropopause responsible for this variation in momentum fluxes are not captured in a WKB framework, as they are neglected by the fundamental WKB assumption of a slowly-varying mean state. Laprise (1993) examined the appropriateness of applying the WKB approximation to linear wave propagation. He found that while the WKB approximation often provided a good estimate of the onset of linear steady-state wave breaking (i.e. where $Nh/U = 1.0$), it often under- or over-estimated the drag significantly compared to a linear steady-state column model. Furthermore, as shown in the semi-analytic analysis in Durran (1992, their Fig. 7), even such linear calculations for complex atmospheric profiles as in Laprise (1993)'s steady-state column model may themselves dramatically over- or under-estimate the momentum fluxes in finite-amplitude non-breaking waves.

The results of Blumen (1965) and Klemp and Lilly (1975) assume discontinuous jumps in static stability. As noted by Blumen (1985) and others, the partial reflection of vertically propagating waves at the tropopause decreases as the thickness of the tropopause transition layer is increased. Teixeira and Argaín (2020) related the decrease in reflection coefficient to the surface pressure drag, and as might be expected, the variation in pressure drag is smaller for larger tropopause thicknesses.

Nevertheless, evidence suggests a discontinuity may often be the best approximation for the tropopause. Birner (2006) constructed a climatology of the fine-scale structure of the tropopause and found that the transition between tropospheric and stratospheric values of static stability is often quite sharp and essentially discontinuous. While a simple discontinuity in static stability can therefore serve as a prototypical model for the tropopause, it is still useful to examine how a smoother tropopause impacts the solution. Teixeira and Argaín (2020) did conduct a preliminary analysis of nonlinear effects on their smooth tropopause solutions, but many of their cases (when dimensionalized with realistic values) result in quite broad tropopause transition layers. In this paper we will extend the investigation in Teixeira and Argaín (2020) to consider thinner and more realistic tropopause transition layers.

Significant vertical variations in $U(z)$ are common during most real-world mountain wave events. Defining the square of the Scorer parameter as

$$l^2 = \frac{N^2}{U^2} - \frac{1}{U}\frac{d^2U}{dz^2}, \tag{2}$$

[1] There are two ways to display streamlines for a mountain-wave linear solution; their differences and our approach are discussed in Appendix B.

the linear, two-dimensional, steady-state Boussinesq wave equation in the presence of vertical wind shear is

$$\left(\frac{\partial^2}{\partial x^2} + \frac{\partial^2}{\partial z^2}\right) w + l^2 w = 0, \tag{3}$$

where w is the vertical velocity. In contrast to the case with constant U and Eq. 1, the nonlinear governing equations cannot be expressed in a form similar to Eq. 3, suggesting that nonlinear effects could be more significant in the presence of shear. While nonlinear effects in the presence of shear have been examined previously by Wells and Vosper (2010), we investigated stronger finite-amplitude effects by simulating higher mountains than the 10 m high ridges considered in their paper.

Since the numerical method used in Durran (1992) was based on two-layer solutions of Long's equation, it is unable to incorporate smooth vertical variations of static stability, which is needed to explore a smooth transition region at the tropopause. It is also unable to incorporate wind shear. To overcome these limitations, we employed a different methodology by linearizing a time-dependent numerical model and comparing its simulations with those of its nonlinear counterpart. This approach allowed us to investigate a much larger space of background profiles than was possible in previous studies.

The rest of the paper proceeds as follows. The linearization of the model and its configuration are described in Section 2. The environmental conditions for the various numerical experiments are described in Section 3. We analyse the results of our simulations in Section 4, and provide further perspective on the way that finite-amplitude effects impact the flow in Section 5. Section 6 contains our conclusions.

2 | MODEL DESCRIPTION

Our nonlinear simulations are performed with the University of Washington meso12 model (Durran and Klemp, 1983) running in a Boussinesq configuration. By neglecting the decrease in mean density with height, the Boussinesq assumption reduces the chance of stratospheric wave breaking in our simulations. This model also serves as the basis for our linearized version. For simplicity in implementing the linearization, we utilize leapfrog time differencing with a Robert-Asselin time filter and fourth order advection in both the linear and nonlinear models.

2.1 | Linearization

For the model to be fully linear, three components must be linearized: the advection terms, the lateral boundary conditions, and the lower boundary condition. The radiation upper boundary condition is already linear (Durran, 2010) and requires no modification. For the basic state, we specify vertically varying but horizontally homogeneous profiles of potential temperature $\bar{\theta}(z)$ and horizontal wind speed $\bar{u}(z)$. The base-state vertical velocity $\bar{w}(z)$ is taken to be identically zero.

In the linear configuration, the coordinate surfaces are flat, and no terrain-following coordinate transformation is required. Letting overbars denote the vertically-varying basic state and primes the perturbations, the advection terms are simply linearized as

$$u_i \frac{\partial s_j}{\partial x_i} = \bar{u}_i \frac{\partial s'_j}{\partial x_i} + u'_i \frac{\partial \bar{s}_j}{\partial x_i} \tag{4}$$

where $(u_1, u_2) = (u, w)$, $(x_1, x_2) = (x, z)$, and $(s_1, s_2, s_3) = (u, w, \theta)$. The outflow boundary conditions are that of

Klemp and Wilhelmson (1978), but with a linearized advection term. For example, at the left boundary, their Equation 2.27,

$$\frac{\partial u}{\partial t} + \left(u + c^*\right) \frac{\partial u}{\partial x} = 0, \tag{5}$$

becomes

$$\frac{\partial u'}{\partial t} + \left(\bar{u} + c^*\right) \frac{\partial u'}{\partial x} = 0. \tag{6}$$

Here c^* is a prescribed outflow phase speed. Waves with this phase speed approaching the boundary are perfectly transmitted through the boundary, while all others are imperfectly transmitted (Durran, 2010).

2.2 | Model Configuration

Our simulations are conducted in two dimensions (x, z) to explore a larger parameter space and also to compare with the two-dimensional two-layer semi-analytic solutions of Durran (1992). However, in contrast to Durran (1992), which used a Witch of Agnesi profile given by

$$h(x) = \frac{h_m a^2}{(x - x_0)^2 + a^2}, \tag{7}$$

where h_m is the mountain crest height, a is the half-width, and x_0 is the centre of the mountain, the terrain profile in our simulations is a $\cos^4$ mountain given by

$$h(x) = \begin{cases} \frac{h_m}{16}\left[1 + \cos\left(\frac{\pi(x-x_0)}{4a}\right)\right]^4, & \left|\frac{(x-x_0)}{4a}\right| < 1 \\ 0, & \left|\frac{(x-x_0)}{4a}\right| \geq 1. \end{cases} \tag{8}$$

A comparison between the $\cos^4$ mountain and the Witch of Agnesi mountain with the same crest height and half-width is shown in Fig. 2. The $\cos^4$ mountain has the advantage that the mountain height drops to zero at a finite distance from the crest. Because of this, all contributions to the surface pressure drag are confined to a small neighbourhood in the centre of the domain. In a constant N and U environment, the linear pressure drag across the $\cos^4$ mountain exceeds that across a Witch of Agnesi with same values of h_m and a by a factor of 1.3. This factor was evaluated numerically from the linear analytic solution using Fourier transforms and confirmed with the time-dependent linearized meso12 model.

For our simulations, the model was run with a horizontal resolution of $\Delta x = 500$ m and a vertical resolution of $\Delta z = 50$ m. The domain was $L_x = 600$ km wide and 30 km tall; the large time step, which is used to integrate all terms not involved in the generation of acoustic modes, was 2 s, and the small time step, used for acoustic modes, was 2/3 s. The Robert-Asselin filter coefficient was set to 0.1. The terrain height was varied between simulations, but the terrain width was specified using a constant $a = 20$ km. The mountain was placed in the centre of the domain at $x_0 = 300$ km in all simulations. The outflow phase speed at the lateral boundaries was specified as $c^* = 35$ m/s at the upstream boundary and $c^* = 15$ m/s at the downstream boundary. These values were chosen to ensure that modes are directed out of the computational domain with appropriate Doppler-shifted phase speeds at both lateral boundaries. The upper boundary used the radiation condition specified in Durran (2010, p. 484), with perfect upward transmission

specified for horizontal wavelengths of 18, 72, and 144 km. Although the model is inviscid, it incorporates scale-selective fourth-derivative dissipation as well as a sub-grid-scale mixing parameterization. This parameterization was active for the nonlinear simulations but inactive for the linear simulations. The background wind field was ramped up from zero to its full value over a period of 4000 s. The model was run to a nondimensional time $U_0 t/a = 43.6$, where U_0 is the surface wind speed, which was long enough for all non-breaking cases to achieve an approximate steady state.

3 | UPSTREAM ENVIRONMENTS

Four families of numerical experiments with differing upstream soundings were conducted in which the heights of the mountain and the tropopause were systematically varied. In the first pair of experiments, where the upstream wind speed is constant with height, the tropopause height varied between $0.3\lambda_L$ and $0.8\lambda_L$ at increments of $0.05\lambda_L$, where $\lambda_L = 2\pi U/N_L$ is the vertical wavelength of a hydrostatic mountain wave in the lower layer (i.e., the troposphere). In the remaining experiments the height of the tropopause varied between 5 km and 15 km in 500 m increments. The mountain height h_m was varied between 100 m and 1000 m in 100 m increments in all experiments. For the first pair of experiments, this corresponds to nondimensional mountain heights $\tilde{h}_m$ from 0.1 to 1.0 with increments of 0.1.

3.1 | Experiment 1: Sharp Tropopause, No Wind Shear

The upper-layer (the stratosphere) has a static stability of $N_U = 0.02\ \mathrm{s}^{-1}$, while the lower layer (the troposphere) has a static stability of $N_L = 0.01\ \mathrm{s}^{-1}$. The wind speed is constant throughout at $U = 20$ m/s.

3.2 | Experiment 2: Gradual Transition at Tropopause

The static stability profile is the same as in the two-layer soundings, except for the presence of a linear transition in N over a depth Δz. For a tropopause height z_T, the static stability profile is given by

$$N(z) = \begin{cases} N_L, & 0 < z < z_T - \frac{\Delta z}{2} \\ N_U, & z > z_T + \frac{\Delta z}{2} \\ \frac{N_L + N_U}{2} + \frac{(N_U - N_L)(z - z_T)}{\Delta z}, & \text{otherwise} \end{cases} \tag{9}$$

Two values of Δz were considered, $\Delta z = 1$ km and $\Delta z = 2$ km. For our values of static stability and wind speed, these correspond to normalized transition layer depths of $0.08\lambda_L$ and $0.16\lambda_L$, respectively.

3.3 | Experiment 3: Sharp Tropopause, 10-30 m/s Shear

The profiles of $U(z)$ are representative of the mid-latitude westerlies, and the static-stability profile is identical to the two-layer structure in Experiment 1. The wind speed increases from 10 m/s at the surface to 30 m/s at the tropopause and drops back to a value of 20 m/s in the stratosphere. An example Experiment-3 profile is shown in Fig. 3 for a case with the tropopause at $z_T = 10$ km. The procedure used to generate $U(z)$ is presented in Appendix A.

3.4 | Experiment 4: Sharp Tropopause, 10-50 m/s Shear

The Experiment-4 soundings are identical to those of Experiment 3, except that the wind speed increases from 10 m/s to 50 m/s in the troposphere. The mid- to upper-stratospheric wind speed remains specified as a constant 20 m/s.

4 | RESULTS

4.1 | Experiment 1: Sharp Tropopause, No Wind Shear

The Experiment-1 soundings admit analytic linear hydrostatic steady-state solutions in wavenumber space, which can be easily transformed to physical space by an inverse Fourier transform. Letting l_L and l_U denote the constant Scorer parameter values below and above the tropopause, the Fourier-transformed vertical velocity field for wavenumber k, $\hat{w}(k,z)$, is given by

$$\hat{w}(k,z) = \begin{cases} a_1 \cos l_L z + b_1 \sin l_L z & 0 < z < z_T \\ a_2 \cos l_U z + b_2 \sin l_U z & z > z_T, \end{cases} \tag{10}$$

where

$$a_1 = Uik\hat{h}, \tag{11}$$

$$b_1 = -\frac{\sin(l_L z_T)\, l_L \beta + \cos(l_L z_T)\, l_U}{\sin(l_L z_T)\, l_U - \cos(l_L z_T)\, l_L \beta} a_1 \tag{12}$$

$$a_2 = a_1 \cos(l_L z_T) + b_1 \sin(l_L z_T), \tag{13}$$

$$b_2 = a_2/\beta \tag{14}$$

$$\beta = \begin{cases} i, & k < 0 \\ -i, & k \geq 0 \end{cases} \tag{15}$$

Here $\hat{h}(k)$ is the Fourier transform of the mountain profile $h(x)$. This is a simplification of the three-layer solution of Klemp and Lilly (1975).

Using the polarization relation

$$\hat{p}(k,z) = -\frac{i\rho_0 U}{k}\frac{\partial \hat{w}}{\partial z} \tag{16}$$

to derive the perturbation pressure $p'(x,z)$ from Eq. 10, the normalized cross-mountain pressure drag

$$\tilde{D}_l = \frac{4}{\pi \rho_0 N_L U h_m^2} \int_0^{L_x} p'(x,0)\frac{\partial h}{\partial x}\, dx. \tag{17}$$

is plotted in Fig. 4 for the $\cos^4$ mountain as a function of the tropopause height nondimensionalized by the vertical wavelength of a hydrostatic mountain wave in the troposphere such that $\tilde{z}_T = N_L z_T/(2\pi U)$. These analytic results may be compared to the drag obtained from a series of linearized meso12 simulations in which p' is replaced in (17) by the steady-state surface pressure from the numerical simulations (orange points in Fig. 4). Although the linearized

meso12 model is nonhydrostatic, we compare directly to the hydrostatic analytic solution because the mountain is wide enough that the response is largely hydrostatic ($a = 20$ km, implying $N_L a/U = 10$ and $N_U a/U = 20$). The pressure drags obtained from linearized meso12 simulations are in close agreement with the analytic solution, thereby providing a check on the correctness of our linearized time-dependent numerical model.

The deviations from the linear uniform-atmosphere pressure drag for the finite-amplitude case are shown in Fig. 5a, in which the normalized drag is contoured as a function of the nondimensional mountain height $\tilde{h}_m = N_L h_m/U$ and $\tilde{z}_T$. Letting $p(x, z)$ be the pressure computed with the nonlinear model at quasi-steady state, the normalized nonlinear pressure drag is

$$\tilde{D}_{nl} = \frac{4}{\pi \rho_0 N_L U h_m^2} \int_0^{L_x} p\,[x, h(x), t]\, \frac{\partial h}{\partial x}\, dx, \tag{18}$$

We define the quasi-steady-state pressure as that occurring at the midpoint of the first interval of duration $\Delta(Ut/a) = 5$ after nondimensional time $Ut/a = 20$ in which the drag varies by less than 5% of the average value within the interval. Note that the normalization factor $\pi\rho_0 N_L U h_m^2/4$ is the drag that would be obtained from many GWD parameterizations, namely the drag generated by linear mountain waves launched by a Witch of Agnesi mountain in an atmosphere with uniform basic-state wind U and static stability N_L. No drag values are plotted in Fig. 5 for those combinations of h_m and z_T that do not achieve quasi-steady state. Breaking waves do not achieve quasi-steady state, and therefore our analysis is restricted to non-breaking waves.

As is well known (Klemp and Lilly, 1975) and evident in Fig. 4, in the limit of small $\tilde{h}_m$ the pressure drag is maximized at $\tilde{z}_T = 0.5$. Fig. 5a shows that, as $\tilde{h}_m$ increases, the maximum $\tilde{D}_{nl}$ occurs at progressively higher tropopause heights, a behaviour consistent with Durran (1992).[2] For $0.15 \leq \tilde{h}_m \leq 0.35$, the maximum values of $\tilde{D}_{nl}$ exceed 2.5, suggesting that use of typical GWD expressions for the drag and momentum flux could be in error by that same factor.

The normalization factor in (18) is for a single-layer atmosphere, not the corresponding linear two-layer problem. Therefore, to isolate the effects of finite amplitude, $\tilde{D}_{nl}/\tilde{D}_l$ is contoured as a function of $\tilde{h}_m$ and $\tilde{z}_T$ in Fig. 5b. Use of the ratio $\tilde{D}_{nl}/\tilde{D}_l$ also removes the factor of roughly 1.3 by which the drag over the $\cos^4$ mountain exceeds that for the reference Witch-of-Agnesi mountain. Linear theory closely approximates the 0.65 to 2.56 range over which the nonlinear pressure drag varies as the tropopause height changes, but the functional dependence on the tropopause height is different in the nonlinear case. Due to the shift of the maximum $\tilde{D}_{nl}$ to increasing tropopause heights as the $\tilde{h}_m$ increases, an amplification-deamplification couplet is present in the field of $\tilde{D}_{nl}/\tilde{D}_l$. For values of $\tilde{z}_T$ above 0.5, $\tilde{D}_{nl}/\tilde{D}_l$ increases with increasing mountain height to its maximum when $(\tilde{h}_m, \tilde{z}_T) = (0.4, 0.65)$, while for $\tilde{z}_T < 0.5$ it decreases as $\tilde{h}_m$ increases, reaching its minimum when $(\tilde{h}_m, \tilde{z}_T) = (0.6, 0.45)$.

A case with strong finite-amplitude amplification ($\tilde{h}_m = 0.3$, $\tilde{z}_T = 0.55$) is illustrated in Fig. 6; vertical velocities and streamlines for the nonlinear solution are shown in Fig. 6b. Relative to the linear solution (Fig. 6a), the nonlinear solution (Fig. 6b) has a much stronger downdraft-updraft couplet over the lee slope, and the lee trough is sharper. These large-amplitude short-wavelength features in the lee trough are not present in the linear simulation because there is little direct forcing at such wavelengths by the wider topography.

A deamplifying case is shown in Fig. 7. While the amplitude of the nonlinear simulation (Fig. 7a) is clearly reduced compared to the linear simulation (Fig. 7b), there are fewer structural differences between the linear and nonlinear solutions than there were in the amplifying case. In particular, the nonlinear solution in the deamplifying case lacks the short-wavelength perturbations in the lee of the ridge which develop in the nonlinear amplifying case (Fig. 6b).

[2] In fact, all of our computed pressure drags are within 3% of those in Durran (1992) once they are adjusted to account for the $\cos^4$ shape of our topography.

4.2 | Experiment 2: Gradual Transition at Tropopause

As might be expected given the results of Teixeira and Argaín (2020), when there is a more gradual transition at the tropopause, the difference between the troposphere-stratosphere solutions and those for a single layer of constant N and U case is reduced. The normalized cross-mountain pressure drag $\tilde{D}_{nl}$ for cases with $\Delta z = 1$ km, shown in Fig. 8a, maintains the general trend of a shift of the peak drag to higher tropopause heights as the mountain height is increased, but the magnitude of the finite-amplitude enhancement is reduced substantially from that apparent in Fig. 5a. The deviation of the nonlinear drag from the linear solution $\tilde{D}_{nl}/\tilde{D}_l$ (Fig. 8b) is also reduced relative to the sharp tropopause result in Fig. 5b, even after accounting for the changes induced in the linear solutions by the more gradual change in static stability at the tropopause.

This lack of sensitivity to finite-amplitude processes is greater in the $\Delta z = 2$ km case. The variation in $\tilde{D}_{nl}$ (Fig. 8c) is smaller than in the $\Delta z = 1$ km case, and there is only a modest trend for the maximum drag to occur at higher tropopause heights as the mountain height increases. The difference between the drag for the linear and nonlinear solutions is particularly small (Fig. 8d).

4.3 | Experiment 3: Sharp Tropopause, 10-30 m/s Shear

When moderate forward shear (cross-mountain wind speed increasing with height) and a sharp tropopause are present, the finite-amplitude enhancement of nonbreaking waves increases relative to the no-shear case. Normalized drag $\tilde{D}_{nl}$ for Experiment 3 is contoured as a function of the dimensional mountain and tropopause heights in Fig. 9a. The dimensional values of h_m and z_T are used in the shear flow cases for easy comparison with observations, and because there is no unique choice for U in the computation of the nondimensional forms. Nevertheless, to facilitate comparison with the previous results we still compute $\tilde{D}_l$ and $\tilde{D}_{nl}$, taking U to be the value at the surface. The range of tropopause heights is sufficiently broad that $\tilde{D}_{nl}$ exhibits a quasi-periodic structure in the tropopause height z_T, with local maxima around 6.5 and 12 km. The values of $\tilde{D}_{nl}$ in these local maxima exhibit the trend seen previously in which there is a shift of the maximum drag to higher tropopause heights as the mountain height increases. The maximum $\tilde{D}_{nl}$ of 5.55 occurs for $h_m = 700$ m, $z_T = 7$ km and is over twice the 2.56 maximum in the no shear case.

In contrast to Experiment 1, nonlinearity almost exclusively acts to increase the pressure drag (Fig. 9b). There are significant regions where $\tilde{D}_{nl}/\tilde{D}_l$ is greater than 2, with a maximum greater than 7. The de-amplification factor, on the other hand, is never less than 1/2. The maximum in $\tilde{D}_{nl}/\tilde{D}_l$ occurs in the case $h_m = 800$ m, $z_T = 8$ km, which is particularly interesting because the linear solution is slightly deamplifying relative to the one-layer linear solution, but the nonlinear solution is strongly amplifying. The linear and nonlinear solutions for this case are compared in Fig. 10. Although they do not directly contribute to the drag, weak partially-trapped waves are present in the nonlinear (Fig. 10b) simulation, while there are none present in the linear case (Fig. 10a). The generation of trapped waves due to short-wavelength forcing in the nonlinear lee wave has been previously well documented (Smith, 1976; Durran and Klemp, 1982).

4.4 | Experiment 4: Sharp Tropopause, 10-50 m/s Shear

When the shear is stronger and $U(z)$ increases from 10 m/s at the surface to 50 m/s at the tropopause, the increase in the local WKB vertical wavelength of hydrostatic mountain waves in the troposphere places the region of maximum amplification in both $\tilde{D}_{nl}$ and $\tilde{D}_{nl}/\tilde{D}_l$ at typical mid-latitude tropopause heights between 9 and 11 km (Fig. 11). The amplification is similar to that for the the weaker shear in Experiment 3, although it occurs at lower mountain heights.

In particular, $\tilde{D}_{nl}$ is greater than 4 when h_m is just 300 m and $z_T = 9$ km. $\tilde{D}_{nl}$ reaches a maximum of 6.6 when $h_m = 700$ m and $z_T = 10$ km, while $\tilde{D}_{nl}/\tilde{D}_l$ exceeds 9.5 when $h_m = 800$ m and $z_T = 11$ km. Very strong nonlinear effects in nonbreaking mountain waves can develop at very small mountain heights when there is strong forward shear in the troposphere.

As in Experiment 3, at most combinations of h_m and z_T, nonlinear effects amplify rather than damp the solution. Vertical velocities and streamlines from the strongly amplifying case $h_m = 800$ m and $z_T = 11$ km are shown in Fig. 12. Leaky trapped waves are pronounced in the nonlinear solution, but as in the previous Experiment 3 with weaker shear, they are absent in the linear case. The vertical velocities and trapped wave amplitudes in the nonlinear Experiment-4 simulation are both significantly stronger than in Experiment 3, despite both cases having equal values of h_m.

5 | DISCUSSION

Neither the free-slip boundary condition at the surface, nor the matching conditions across the tropopause (requiring continuity of the pressure and the normal component of the velocity) are nonlinear in the unknown variables. Durran (1992) noted there is an effective reduction in the depth of the troposphere over finite-amplitude mountains, and found that tropopause heights giving the strongest drag can be adjusted to capture this finite-amplitude behaviour by generalizing the tuning criteria for maximum drag in linear hydrostatic mountain waves from $z_T = 0.5\lambda_L$ to $z_T - 1.5h_m = 0.5\lambda_L$. A similar adjustment works well over the wider range of mountain heights and tropopause elevations considered in our no-shear simulations, for which normalized drags are plotted in Fig. 5a along with a dashed line following the extrema in $\tilde{D}_{nl}$ given by $z_T - 1.17h_m = 0.5\lambda_L$ (fit by eye; note that this is close to simply calculating the tropopause height as the distance above the mountain top, instead of the surrounding flat ground). Plotting $\tilde{D}_{nl}$ as a function of mountain height *along this dashed line* yields the almost-horizontal blue curve in Fig. 13, indicating that linear theory for the two-layer problem can give the correct drag, at least for the strongest events, after making a finite-amplitude adjustment to the depth of the troposphere.

Similar attempts to apply two-layer linear theory via a simple adjustment of the effective depth of the troposphere did not, however, work well for the cases with vertical wind shear. Dashed lines indicating the approximate (h_m, z_T) values for which $\tilde{D}_{nl}$ achieves a local maximum appear in Figs. 9a and 11a; the normalized pressure drags along these curves are plotted as a function of h_m in Fig. 13. These curves are not quasi-horizontal, but rather indicate that, in the wind-shear simulations, a significant amplification of $\tilde{D}_{nl}$ occurs beyond that which can be accounted for by simple reductions in the tropospheric depth above finite-amplitude mountains.

The additional amplification of the drag in the wind-shear cases is associated with a significant nonlinear strengthening of the lee-side trough, as may be illustrated by plotting the local contribution to the pressure drag $p'\, dh/dx$ at each point on the topography. Fig. 14 shows the behaviour of this local drag for three different environments: no-shear with $z_T = 8.16$ km ($\tilde{z}_T = 0.65$), winds increasing from 10 to 30 m s^{-1} with $z_T = 8$ km, and winds increasing from 10 to 50 m s^{-1} with $z_T = 11$ km. Individual curves for mountain heights of 200, 400, 600, and 800 m are plotted for each environmental profile. In all three cases, the largest contribution to the pressure drag occurs along the lee slopes as a result of low surface pressures under the lee-side trough. The increase in the amplitude of this lee-side contribution, as h_m increases from 400 to 600 to 800 m, is much more pronounced in the two cases with wind shear. In those cases the rate at which the drag increases with h_m is also much faster than the h_m^2 scaling that would be expected from linear theory if the influence of finite mountain height on the effective tropospheric depth is neglected.

Streamlines and vertical velocities for the linear and nonlinear $h_m = 800$-m, 10-30 m s^{-1} simulations are compared in Fig. 10. The dramatic intensification of the lee trough responsible for the increased local drag in Fig. 14b is clearly

apparent. Nonlinear wave interactions have substantially amplified short-wavelength contributions to the wave downstream of the trough axis. At a height of $z = 2$ km, the half wavelength between the trough and the downstream ridge ($325 \leq x \leq 340$) is approximately 15 km. The terrain itself is too wide to directly force strong 30-km-wavelength perturbations—instead they are forced by the nonlinear wave dynamics. A similar situation is apparent for the 10-50 m s^{-1} simulations shown in Fig. 12, for which the local drag contribution is plotted in Fig. 14c.

Smith (1976) proposed that nonlinear flow over barrier can trigger a strong, short wavelength trough, thereby forcing larger-amplitude lee waves downstream than those which would be obtained from a linear calculation. Further evidence of such nonlinear amplification appears in Durran (1992, 2015), and in all the cases in these previous studies, the environmental profile supporting the trapped waves has a two-layer structure with high static stability in the lower layer. In contrast to these previous studies, the decrease in the Scorer parameter with height responsible for partially trapping the waves in Figs. 10b and 12b is produced by the increase in U with height without any variation of the static stability within the troposphere.

The vertical structures of the partially trapped waves supported by the environmental profiles of the Scorer parameter in the shear-flow cases in Figs. 10 and 12 were evaluated using the eigenvalue-eigenfunction solver described in Durran et al. (2015) as modified in Metz et al. (2020). Fig. 15a,c shows the vertical profile of the Scorer parameter squared for the 10-30 and 10-50 m s^{-1} shear flows, respectively, while Fig. 15b,d illustrates their modal structures by profiles of $\hat{w}(z)$, defined such that $w(x,z) = \mathrm{Re}\left(\hat{w}(z)e^{ikx}\right)$. Also noted in panels b and d are the horizontal wavelengths $\lambda_x = 2\pi/k$ for each mode and their downstream decay rate D_λ, defined as the fraction of the wave amplitude lost over a distance λ_x. The upper-tropospheric layer throughout which $l^2 < k^2$, and the waves decay, is only a few kilometres deep (the layer just below the tropopause where the red curve lies to the left of the blue line in Fig. 15a,c), so it is not surprising that both modes decay rapidly downstream as they leak energy upward, losing roughly 38% and 30% of their amplitude over one horizontal wavelength. The wavelengths and vertical structure of the downstream waves in the numerical simulations closely match those shown in Fig. 15.

The extent to which these partially trapped modes contribute to the drag is unclear. The ability of trapped waves to exert a drag on the flow was demonstrated in the classic paper by Bretherton (1969), yet the trapped waves themselves do not transport momentum vertically. Rather their interaction with the mountain produces a vertical divergence in the horizontally averaged momentum flux (Durran, 1995; Lott, 1998; Broad, 2002). The situation for these rapidly decaying waves that do transport momentum vertically (note the sinusoidal oscillations in the stratosphere in Fig. 15b,d) is more complex and needs further study. Nevertheless, the pronounced amplification of these waves clearly illustrates the consequences of the nonlinear scale interactions in the high-drag simulations with significant vertical shear.

6 | CONCLUSIONS

Our simulations have demonstrated that mountain waves encountering a sharp tropopause can experience large changes in amplitude and substantial deviations in momentum flux compared to that which would be present in an environment with constant values of N and U representative of the conditions near mountain-top level. Many GWD parameterizations will, therefore, be in error because they assume the low-level momentum flux is proportional to the constant-N-and-U drag in linear waves launched by the unblocked flow over the top of the ridge. Note in particular that large deviations between constant-N-and-U GWD estimates and the actual momentum fluxes can occur at amplitudes below the wave-breaking threshold.

Linear theory is often applied to the mountain wave problem using WKB theory, but that theory assumes a slowly

varying background state that is violated at a sharp tropopause. Linear theory can alternatively be formulated for distinct atmospheric layers with matching conditions between the layers, including cases with linear variations in $U(z)$ within each layer (Klemp and Lilly, 1975), thereby allowing a reasonably close match to observed sounding profiles. Nevertheless, our results suggest that the finite-amplitude solutions can differ dramatically from such multi-layer linear solutions, which is consistent with previous findings in the more limited case without vertical wind shear (Durran, 1992). The differences between the linear and finite-amplitude results are large enough that there would be little reason to try to incorporate complex multi-layer linear models with vertical wind shear in GWD parameterizations.

In the simplest two-layer case with no vertical wind shear, linear theory accurately predicts the range over which the drag varies in response to changes in the tropopause height, but the functional dependence on z_T is incorrect. Finite-amplitude effects tend to shift the extrema in the drag to higher tropopause heights as the mountain height increases, decreasing the effective depth of the troposphere (Fig. 5). Similar to Durran (1992), the optimal tropopause height for maximum drag could be estimated by empirically correcting the condition from linear theory through the inclusion of a term proportional to the mountain height. We also demonstrated that, at least for the strongest cases, good estimates of the finite-amplitude drag could also be obtained from linear theory using the same empirical correction.

The sensitivity of the surface pressure drag to finite-amplitude effects increases when the cross-mountain winds increase with height. In this case, multi-layer linear theory does not accurately predict the range of possible pressure drags. For example, in the 10-30 m/s shear case, $\tilde{D}_l$ ranges from approximately 0.5 to 3.0, while $\tilde{D}_{nl}$ varies from 0.5 to 4.8. In the 10-50 m/s shear case, strong nonlinear amplification relative to typical GWD estimates can occur over mountains that are just 250 m high (Fig. 11a). Nonlinear dynamics are important in the high-drag cases with wind shear, and it is not possible to obtain good agreement with linear theory by simply compensating for changes in the effective tropospheric depth above finite-height topography. Leaky trapped waves appear in the high-drag simulations with significant wind shear, triggered by short-wavelength structures in the lee-trough immediately downstream of the mountain. These waves match the vertical-mode structure of the leaky modes supported by the oncoming background flow as computed using linear theory. The strong nonlinear response in vertically sheared environments is qualitatively similar to that previously documented in cases where a significant decrease in the Scorer parameter with height is produced, not by increases in wind speed, but by decreases in the upper tropospheric static stability (Durran, 1986). The influence of these leaky waves on the drag, and the influence of the tropopause on these leaky waves, are topics for further study.

An important additional influence of vertical shear, due to the change in the vertical wavelength from the varying wind speed, is to modulate the level at which the drag is most sensitive to partial reflections from the tropopause. The dry Brunt-Väisälä frequency, averaged over the full depth of the troposphere, is usually near 0.01 s^{-1}. Given an N_L of 0.01 s^{-1}, an environmental wind profile in which $U(z)$ increases linearly from 10 m/s near the surface to 50 m/s at the tropopause will be conducive to very strong nonlinear amplification of the mountain-wave drag when z_T has a typical mid-latitude value in the range between 8 and 11 km.

We have focused on the impact of partial back reflections of vertically propagating waves at the tropopause, and on the influence of strong vertical wind shear, because they are ubiquitous mid-latitude features (Birner, 2006). Other sharp changes in atmospheric structure, such as the presence of an inversion layer near mountain top-level, are also known to have a strong influence on the amplitude of mountain waves (Durran, 1986, Figs. 10-13), and these influences extend into the wave-breaking regime. A thorough analysis in the influence of elevated inversions and the behaviour of breaking mountain waves in environments with wind shear and static-stability layering is beyond the scope of this paper. Nevertheless, our results demonstrate that finite-amplitude effects in mountain waves cannot be reliably accounted for without numerically computing the actual wave response. As a consequence, the associated

gravity-wave drag is not easily parameterized, and errors due to improper representation of GWD in global weather and climate models are likely to remain nontrivial unless the grid spacing becomes small enough to resolve the waves. The current efforts to develop and migrate to global cloud-resolving models could provide the required numerical resolution and thereby promise to improve representation of orographic wave drag (Satoh et al., 2019).

A | GENERATION OF SHEAR SOUNDINGS

The shear soundings are constructed differently in the troposphere than in the stratosphere. In the troposphere, we specify $N = 0.01\,\mathrm{s}^{-1}$ and linear shear

$$U(z) = \frac{U_T - 10\,\mathrm{m/s}}{z_T} z + 10\,\mathrm{m/s}, \tag{19}$$

where z_T is the height of the tropopause and U_T is the wind speed at the tropopause. In the stratosphere, we employ a more complex procedure designed to obtain a smooth profile that eventually transitions to a constant value of $U_S = 20\,\mathrm{m/s}$. Note that the definition of the Scorer parameter (Eq. 2) can be rearranged as a second order nonlinear ordinary differential equation for the basic-state wind speed U:

$$\frac{d^2U}{dz^2} - \frac{N^2}{U} + Ul^2 = 0. \tag{20}$$

This equation can be solved numerically as an "initial value problem" in the height variable z, for which purpose we use the SciPy `odeint` function. Defining $\zeta = z - z_T$, we specify $U(\zeta = 0) = U_T$ and $U'(\zeta = 0) = (U_T - 10\,\mathrm{m/s})/z_T$. In addition, we specify a constant value for the Scorer parameter, $l = 0.02/U_m\ \mathrm{m}^{-1}$, where $U_m = (U_T + 20)/2$ is chosen as the average of the wind speed at the tropopause and the constant upper-stratospheric value.

Specifying N^2 will completely specify the profile of U. However, in general, a constant value of N in the stratosphere will result in large sinusoidal variations in U with height. To prevent this, we still specify a constant value of $N = 0.02\,\mathrm{s}^{-1}$, but we transition from the oscillatory wind profile to a constant U profile by fitting an elliptic wind profile in between. The wind profile in the elliptic transition region is given by

$$U_e(z) = U_0 + \sqrt{a^2\left[1 - \frac{(z - z_0)^2}{b^2}\right]}. \tag{21}$$

This equation has four free parameters: the U- and z-coordinates of the centre of the ellipse U_0 and z_0 and the length of the semi-major and semi-minor axes a and b. We in turn specify four matching conditions, two at each boundary of the elliptic transition region. The lower boundary is specified as being at the first point $z = z_i$ above the tropopause where the curvature of the wind profile is zero, while the upper boundary is specified to be $\Delta z = 3\,\mathrm{km}$ above the lower boundary. At both of these points we require that both the wind profile and the first derivative be continuous. The resulting equations for each parameter are given by

$$U_0 = \frac{U(z_i)\,U'(z_i)\,\Delta z + U(z_i)^2 - U_S^2}{U'(z_i)\,\Delta z + 2\left[U(z_i) - U_S\right]}, \tag{22}$$

$$a^2 = (U_S - U_0)^2, \text{ and} \tag{23}$$

$$b^2 = \frac{(U_0 - U_S)^2 \, \Delta z^2}{2U(z_i)\, U_0 - U(z_i)^2 - 2U_S U_0 + U_S^2}, \tag{24}$$

where $U_S = 20\,\mathrm{m\,s^{-1}}$ is the constant wind speed above the transition region, $\Delta z = 3$ km is the thickness of the transition region, and $U(z_i)$ and $U'(z_i)$ is the wind speed and first derivative of the wind speed at the lower boundary z_i of the transition region. An example result from this procedure is shown in Fig. 16.

B | COMPUTATION OF LINEAR STREAMLINES

Linear solutions are obtained by assuming all perturbations about a reference state are arbitrarily small. Under this small-amplitude assumption, the vertical excursions of streamlines about a horizontal reference line would be infinitesimal, and they would simply appear as horizontal lines. The amplitude of linear solutions is scaled up when approximating the flow over a finite-amplitude mountain, but this leads to an inconsistency between two possible ways to display the streamlines.

Streamlines in the 2D x-z plane satisfy

$$\frac{dz}{dx} = \frac{w}{u}. \tag{25}$$

In the standard finite-amplitude computation, the velocities on the right side of the preceding are evaluated at each point along the streamline, in which case the (x, z) coordinates of a streamline originating at the point (x_0, z_0) may be computed as a function of the parameter s using

$$x(s) = x_0 + \int_0^s u\left(x(\alpha), z(\alpha)\right) d\alpha \tag{26}$$

$$z(s) = z_0 + \int_0^s w\left(x(\alpha), z(\alpha)\right) d\alpha. \tag{27}$$

Streamlines computed in this manner are plotted in red in Fig. 17 for one-layer constant-N-and-U linear flow over a Witch-of-Agnesi mountain. Note that the surface streamline does not follow the mountain profile (shown in blue). For steady adiabatic flow, this procedure generates lines identical to those that would be obtained by applying a standard contouring algorithm to the potential temperature field. As with streamlines, if isentropes are plotted in this manner, they will not coincide with the mountain profile.

To obtain a streamline that follows the mountain, it is necessary to return to the small-amplitude assumption by neglecting the functional dependence of u and w on the amplitude of the streamline displacement. This requires replacing $z(\alpha)$ in Eq. 26 and 27 with z_0. Consistent with the linearization assumption, u must be approximated by the basic-state horizontal velocity U. The coordinates $(\tilde{x}, \tilde{y})$ of such streamlines satisfy

$$\tilde{x}(s) = x_0 + U(z_0)s \tag{28}$$

$$\tilde{z}(s) = z_0 + \int_{x_0}^s w\left[\tilde{x}(\alpha), z_0\right] d\alpha. \tag{29}$$

Streamlines plotted using Eqs. 28 and 29 are shown in black in Fig. 17. The surface streamline perfectly follows the mountain contour, and is identical to the blue curve. Over the mountain, the magnitudes of the slopes of the black streamlines are similar around $z = 2.3$ and 4.6 km, but they are opposite in sign. In contrast, the red streamlines are much steeper than the black streamlines at 4.6 km, and less steep at 2.3 km. *In this case where U is constant with height, the red lines are actually streamlines for the solution to Long's equation (Eq. 1) for flow over a mountain whose profile matches the lowest red streamline in Fig. 17.*

We have used Eqs. 28 and 29 in all plots of linear solutions in this paper because in most respects this choice more faithfully represents the linear solution. But there is one drawback to this approach: when the amplitude is sufficiently large and the streamline spacing is sufficiently tight, sets of $(\tilde{x}, \tilde{z})$ streamlines can cross. Such crossing streamlines are a manifestation of the inconsistency resulting from computing solutions under an assumption of infinitesimal amplitude and then scaling up the amplitude of the result.

Acknowledgements

The authors benefited from discussion with Jim Doyle. This research was supported by National Science Foundation grant AGS-1929466.

References

Birner, T. (2006) Fine-scale structure of the extratropical tropopause region. *Journal of Geophysical Research: Atmospheres*, **111**.

Blumen, W. (1965) Momentum Flux by Mountain Waves in a Stratified Rotating Atmosphere. *Journal of the Atmospheric Sciences*, **22**, 529–534.

— (1985) Reflection of Hydrostatic Gravity Waves in a Stratified Shear Flow. Part I: Theory. *Journal of the Atmospheric Sciences*, **42**, 2255–2263.

Bretherton, F. P. (1969) Momentum transport by gravity waves. *Quart. J. Roy. Meteor. Soc.*, **95**, 213–243.

Broad, A. S. (2002) Momentum flux due to trapped waves forced by mountains. *Quart. J. Roy. Meteor. Soc.*, **128**, 2167–2173.

Chen, J.-H., Lin, S.-J., Magnusson, L., Bender, M., Chen, X., Zhou, L., Xiang, B., Rees, S., Morin, M. and Harris, L. (2019) Advancements in Hurricane Prediction With NOAA's Next-Generation Forecast System. *Geophysical Research Letters*, **46**, 4495–4501.

Choi, H.-J. and Hong, S.-Y. (2015) An updated subgrid orographic parameterization for global atmospheric forecast models. *Journal of Geophysical Research: Atmospheres*, **120**, 2015JD024230.

Durran, D. R. (1986) Another Look at Downslope Windstorms. Part I: The Development of Analogs to Supercritical Flow in an Infinitely Deep, Continuously Stratified Fluid. *Journal of the Atmospheric Sciences*, **43**, 2527–2543.

— (1992) Two-Layer Solutions to Long's Equation For Vertically Propagating Mountain Waves: How Good Is Linear Theory? *Quarterly Journal of the Royal Meteorological Society*, **118**, 415–433.

— (1995) Do Breaking Mountain Waves Decelerate the Local Mean Flow? *Journal of the Atmospheric Sciences*, **52**, 4010–4032.

— (2010) *Numerical Methods for Fluid Dynamics with Applications to Geophysics*. Texts in Applied Mathematics ; 32. New York: Springer, 2nd ed. edn.

— (2015) Lee waves and mountain waves. In *Encyclopedia of Atmospheric Sciences* (ed. G. R. North), 95–102. Elsevier Ltd., 2nd edn.

Durran, D. R., Hills, M. O. G. and Blossey, P. N. (2015) The Dissipation of Trapped Lee Waves. Part I: Leakage of Inviscid Waves into the Stratosphere. *Journal of the Atmospheric Sciences*, **72**, 1569–1584.

Durran, D. R. and Klemp, J. B. (1982) The Effects of Moisture on Trapped Mountain Lee Waves. *Journal of the Atmospheric Sciences*, **39**, 2490–2506.

— (1983) A Compressible Model for the Simulation of Moist Mountain Waves. *Monthly Weather Review*, **111**, 2341–2361.

ECMWF (2020) Part IV: Physical Processes. In *IFS Documentation CY47R1*, no. 4 in IFS Documentation. ECMWF.

Eliassen, A. and Palm, E. (1960) Wave energy transfer in stationary gravity waves. *Geofys. Publ.*, **22**.

Guest, F. M., Reeder, M. J., Marks, C. J. and Karoly, D. J. (2000) Inertia–Gravity Waves Observed in the Lower Stratosphere over Macquarie Island. *Journal of the Atmospheric Sciences*, **57**, 737–752.

Kim, Y.-J. and Arakawa, A. (1995) Improvement of Orographic Gravity Wave Parameterization Using a Mesoscale Gravity Wave Model. *Journal of the Atmospheric Sciences*, **52**, 1875–1902.

Kim, Y.-j. and Doyle, J. D. (2005) Extension of an orographic-drag parametrization scheme to incorporate orographic anisotropy and flow blocking. *Quarterly Journal of the Royal Meteorological Society*, **131**, 1893–1921.

Kim, Y.-J., Eckermann, S. D. and Chun, H.-Y. (2003) An overview of the past, present and future of gravity-wave drag parametrization for numerical climate and weather prediction models. *Atmosphere-Ocean*, **41**, 65–98.

Klemp, J. B. and Lilly, D. K. (1975) The Dynamics of Wave-Induced Downslope Winds. *Journal of the Atmospheric Sciences*, **32**, 320–339.

Klemp, J. B. and Wilhelmson, R. B. (1978) The Simulation of Three-Dimensional Convective Storm Dynamics. *Journal of the Atmospheric Sciences*, **35**, 1070–1096.

Laprise, J. P. R. (1993) An Assessment of the WKBJ Approximation to the Vertical Structure of Linear Mountain Waves: Implications for Gravity-Wave Drag Parameterization. *Journal of the Atmospheric Sciences*, **50**, 1469–1487.

Long, R. R. (1953) Some Aspects of the Flow of Stratified Fluids: I. A Theoretical Investigation. *Tellus*, **5**, 42–58.

Lott, F. (1998) Linear mountain drag and averaged pseudo-momentum flux profiles in the presence of trapped lee waves. *Tellus*, **50A**, 12–25.

Lott, F. and Miller, M. J. (1997) A new subgrid-scale orographic drag parametrization: Its formulation and testing. *Quart. J. Roy. Meteor. Soc.*, **123**, 101–127.

Marks, C. J. and Eckermann, S. D. (1995) A Three-Dimensional Nonhydrostatic Ray-Tracing Model for Gravity Waves: Formulation and Preliminary Results for the Middle Atmosphere. *Journal of the Atmospheric Sciences*, **52**, 1959–1984.

McFarlane, N. (1987) The effect of orographically excited gravity wave drag on the general circulation of the lower stratosphere and troposphere. *J. Atmos. Sci.*, **44**, 1775–1800.

Metz, J. J., Durran, D. R. and Blossey, P. N. (2020) Unusual Trapped Mountain Lee Waves with Deep Vertical Penetration and Significant Stratospheric Amplitude. *Journal of the Atmospheric Sciences*, **77**, 633–646.

Palmer, T., Shutts, G. and Swinbank, R. (1986) Alleviation of a systematic westerly bias in general circulation and numerical weather prediction models through an orographic gravity wave drag parametrization. *Quart. J. Roy. Meteor. Soc.*, **112**, 1001–1039.

Queney, P. (1948) The Problem of Air Flow Over Mountains: A Summary of Theoretical Studies. *Bulletin of the American Meteorological Society*, **29**, 16–26.

Sandu, I., Bechtold, P., Beljaars, A., Bozzo, A., Pithan, F., Shepherd, T. G. and Zadra, A. (2016) Impacts of parameterized orographic drag on the Northern Hemisphere winter circulation. *Journal of Advances in Modeling Earth Systems*, **8**, 196–211.

Satoh, M., Stevens, B., Judt, F., Khairoutdinov, M., Lin, S.-J., Putman, W. M. and Düben, P. (2019) Global Cloud-Resolving Models. *Current Climate Change Reports*, **5**, 172–184.

Scinocca, J. F. and McFarlane, N. A. (2000) The parametrization of drag induced by stratified flow over anisotropic orography. *Quarterly Journal of the Royal Meteorological Society*, **126**, 2353–2393.

Scorer, R. (1949) Theory of waves in the lee of mountains. *Quart. J. Roy. Meteor. Soc.*, **75**, 41–56.

Smith, R. B. (1976) The Generation of Lee Waves by the Blue Ridge. *Journal of the Atmospheric Sciences*, **33**, 507–519.

Smith, R. B. and Kruse, C. G. (2017) Broad-Spectrum Mountain Waves. *Journal of the Atmospheric Sciences*, **74**, 1381–1402.

Smith, R. B., Nugent, A. D., Kruse, C. G., Fritts, D. C., Doyle, J. D., Eckermann, S. D., Taylor, M. J., Dörnbrack, A., Uddstrom, M., Cooper, W., Romashkin, P., Jensen, J. and Beaton, S. (2016) Stratospheric Gravity Wave Fluxes and Scales during DEEPWAVE. *Journal of the Atmospheric Sciences*, **73**, 2851–2869.

Smith, R. B., Woods, B. K., Jensen, J., Cooper, W. A., Doyle, J. D., Jiang, Q. and Grubišić, V. (2008) Mountain Waves Entering the Stratosphere. *Journal of the Atmospheric Sciences*, **65**, 2543–2562.

Teixeira, M. A. C. and Argaín, J. L. (2020) The dependence of mountain wave reflection on the abruptness of atmospheric profile variations. *Quarterly Journal of the Royal Meteorological Society*, **146**, 1685–1701.

Walters, D., Brooks, M., Boutle, I., Melvin, T., Stratton, R., Vosper, S., Wells, H., Williams, K., Wood, N., Allen, T., Bushell, A., Copsey, D., Earnshaw, P., Edwards, J., Gross, M., Hardiman, S., Harris, C., Heming, J., Klingaman, N., Levine, R., Manners, J., Martin, G., Milton, S., Mittermaier, M., Morcrette, C., Riddick, T., Roberts, M., Sanchez, C., Selwood, P., Stirling, A., Smith, C., Suri, D., Tennant, W., Vidale, P. L., Wilkinson, J., Willett, M., Woolnough, S. and Xavier, P. (2017) The Met Office Unified Model Global Atmosphere 6.0/6.1 and JULES Global Land 6.0/6.1 configurations. *Geoscientific Model Development*, **10**, 1487–1520.

Wells, H. and Vosper, S. B. (2010) The accuracy of linear theory for predicting mountain-wave drag: Implications for parametrization schemes. *Quarterly Journal of the Royal Meteorological Society*, **136**, 429–441.

Zhou, L., Lin, S.-J., Chen, J.-H., Harris, L. M., Chen, X. and Rees, S. L. (2019) Toward Convective-Scale Prediction within the Next Generation Global Prediction System. *Bulletin of the American Meteorological Society*, **100**, 1225–1243.

List of Figures

1 Comparison of streamlines of the one-layer linear (black) and nonlinear (red) solutions for a Witch of Agnesi mountain with $a = 10\,\mathrm{km}$ and $Nh_m/U = 0.6$. Airflow is left to right; the mountain profile is shown in blue. 20

2 Comparison of a $\cos^4$ (blue) and a Witch of Agnesi (orange) profile with the same values of h_m and a. . 21

3 Vertical profiles of (a) Brunt-Väisälä frequency N and (b) horizontal wind speed U for an Experiment-3 case with the tropopause height set at 10 km. 22

4 Cross-mountain pressure drag $\tilde{D}_l$ as a function of nondimensional tropopause height $\tilde{z}_T$ for Experiment 1 computed by the semi-analytic method (blue line) and using the linearized meso12 model run to steady state (orange points). 23

5 (a) Normalized cross-mountain pressure drag $\tilde{D}_{nl}$ for the Experiment-1 simulations contoured as a function of nondimensional mountain and tropopause heights, and (b) Amplification of the nonlinear drag relative to that for the corresponding linear solution. The linear solution is plotted at a mountain height of 0.0. The thick black line indicates a normalized pressure drag or amplification of 1.0. White areas are plotted for those values of $\tilde{h}_m$ and $\tilde{z}_T$ that produce breaking mountain waves. The black dashed line, satisfying $\tilde{z}_T = 1.17\tilde{h}_m + 0.5$, is an empirical fix to the set of $(\tilde{h}_m, \tilde{z}_T)$ along which $\tilde{D}_{nl}$ is maximized and is discussed in connection with Fig. 13. 24

6 Vertical velocity (colour fill) and streamlines (black lines) from the (a) linear and (b) nonlinear meso12 simulations of an Experiment-1 case with nonlinear amplification in which $\tilde{z}_T = 0.55\lambda_L$ and $\tilde{h}_m = 0.3$. The grey line indicates the tropopause, and grey stippling indicates the stratosphere. 25

7 As in Fig. 6, but for a case with nonlinear deamplification in which $\tilde{z}_T = 0.45\lambda_L$ and $\tilde{h}_m = 0.6$. 26

8 Normalized drag $\tilde{D}_{nl}$ as in Fig. 5a for the Experiment-2 simulations with (a) $\Delta z = 1\,\mathrm{km}$ and (c) $\Delta z = 2\,\mathrm{km}$. Amplification of the drag relative to the linear solution $\tilde{D}_{nl}/\tilde{D}_l$ as in Fig. 5b for cases with (b) $\Delta z = 1\,\mathrm{km}$ and (d) $\Delta z = 2\,\mathrm{km}$. 27

9 (a) Normalized drag $\tilde{D}_{nl}$ and amplification of the drag relative to the linear solution $\tilde{D}_{nl}/\tilde{D}_l$, as in Fig. 5, for the Experiment-3 simulations. 28

10 As in Fig. 6, but for the 10 m/s to 30 m/s shear sounding with a tropopause height of $z_T = 8\,\mathrm{km}$ and a mountain height of $h_m = 800\,\mathrm{m}$. 29

11 (a) Normalized drag $\tilde{D}_{nl}$ and amplification of the drag relative to the linear solution $\tilde{D}_{nl}/\tilde{D}_l$, as in Fig. 5, for the Experiment-3 simulations. 30

12 As in Fig. 6, but for Experiment 4 with $h_m = 800\,\mathrm{m}$ and $z_T = 11\,\mathrm{km}$. 31

13 Normalized pressure drag as a function of mountain height along the dashed lines in Figs. 5a, 9a and 11a for the no-shear case (blue), the lower-level/upper-level maximum in the 10-30 m/s case (green/orange), and for the 10-50 m/s case (red). 32

14 Local pressure drag for the (a) no-shear case, (b) 10-30 m/s shear case, and (c) 10-50 m/s shear case. Blue, orange, green, and red lines are for mountain heights of 200 m, 400 m, 600 m, and 800 m, respectively. Tropopause heights are $\tilde{z}_T = 0.65$ for the no-shear case and $z_T = 8\,\mathrm{km}$ and $z_T = 11\,\mathrm{km}$ for the 10-30 m/s and 10-50 m/s shear cases, respectively. For reference, the mountain profile is plotted as a black dashed line. 33

15 Vertical profiles of (a, c) Scorer parameter l squared (red) and (b, d) real part of the Fourier-transformed vertical velocity $\hat{w}(z)$ for the trapped wave mode supported by the (a, b) 10-30 m/s shear case with a tropopause height of 8 km and (c, d) 10-50 m/s shear case with a tropopause height of 11 km. The horizontal wavenumber k of this mode is plotted as the blue vertical line in (a, c). The grey shading in (b, d) indicates the interval $[-|\hat{w}|, |\hat{w}|]$, where $|\hat{w}|$ is the magnitude of $\hat{w}$. The parameters λ_x and D_λ indicate the horizontal wavelength and downstream decay per wavelength, respectively. 34

16 Demonstration of the construction of a wind profile in the stratosphere. The blue curve indicates the solution for a constant Scorer parameter l. The red dot indicates the first point with zero curvature above the tropopause, while the green curve indicates the ellipse used to transition between the constant-l and constant-U profiles. The resulting wind profile is shown in black. 35

17 Comparison between two methods of plotting linear streamlines in flow from left to right over a Witch of Agnesi mountain: red lines use Eqs. 26 and 27; black lines use Eqs. 28 and 29. The mountain profile is shown in blue and coincides with the lowest black streamline. 36

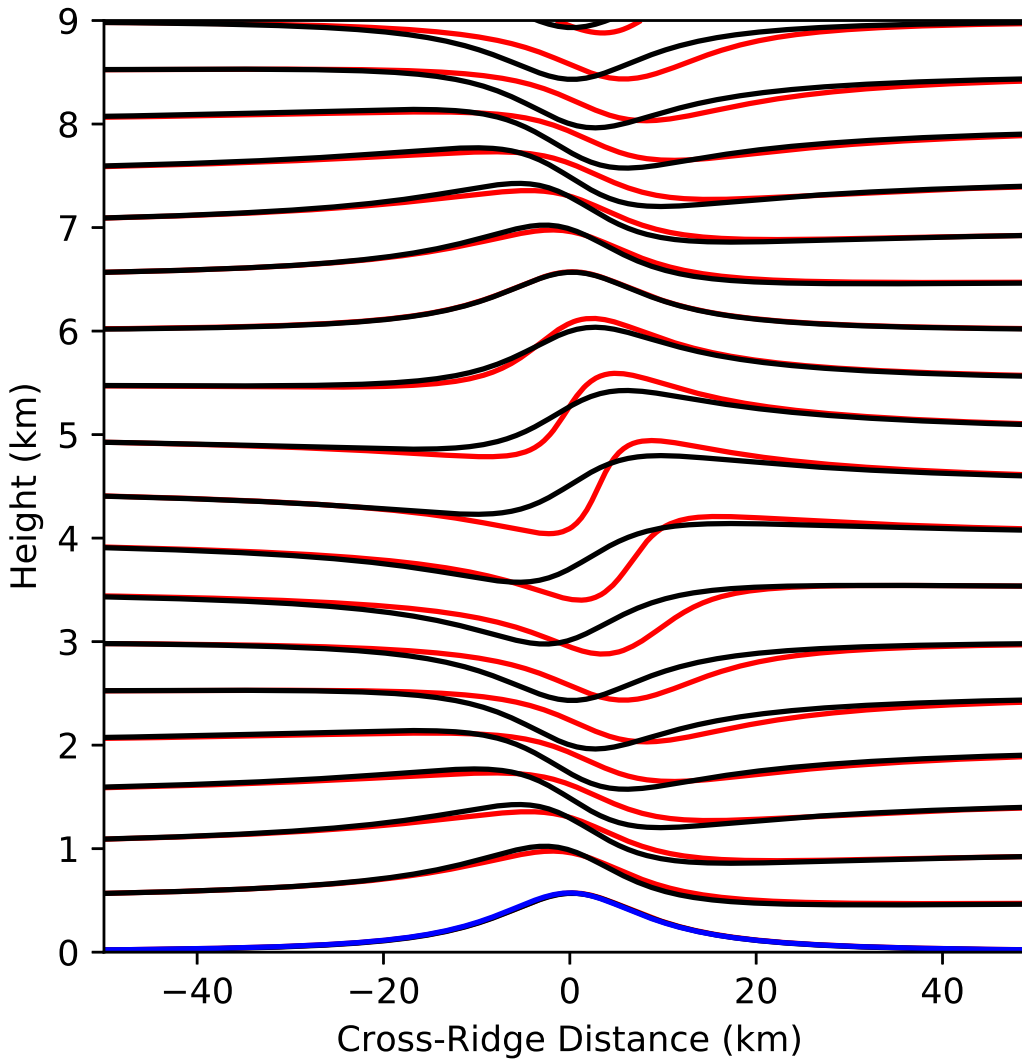

FIGURE 1 Comparison of streamlines of the one-layer linear (black) and nonlinear (red) solutions for a Witch of Agnesi mountain with $a = 10\,\mathrm{km}$ and $Nh_m/U = 0.6$. Airflow is left to right; the mountain profile is shown in blue.

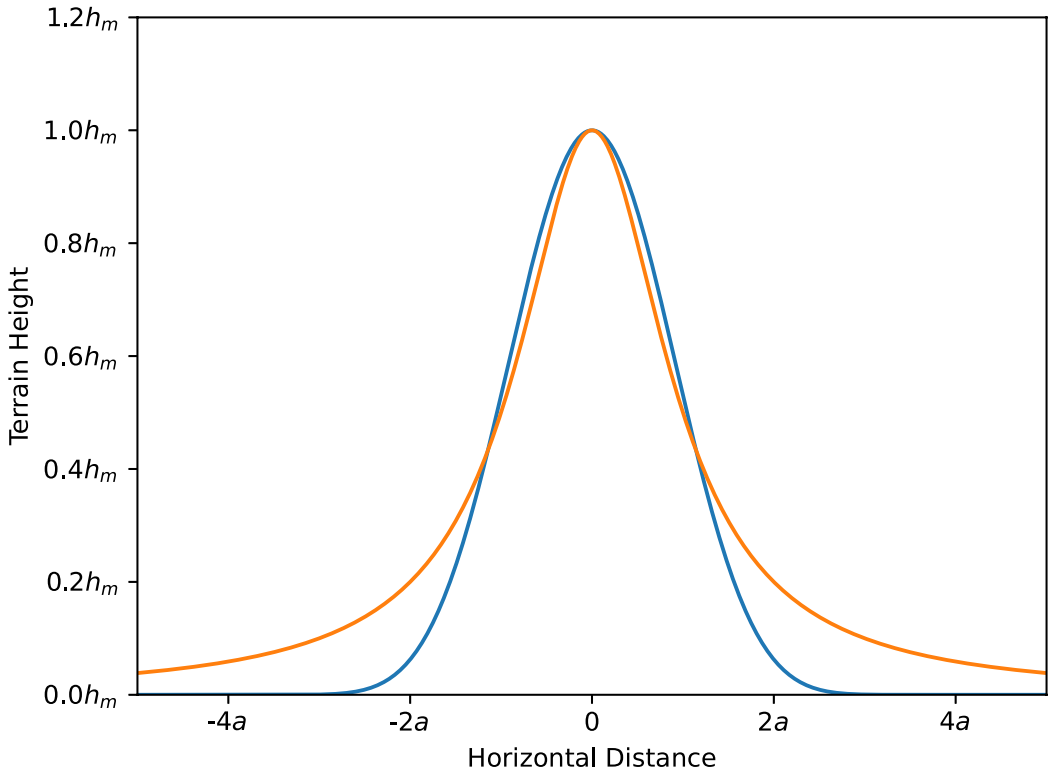

FIGURE 2 Comparison of a $\cos^4$ (blue) and a Witch of Agnesi (orange) profile with the same values of h_m and a.

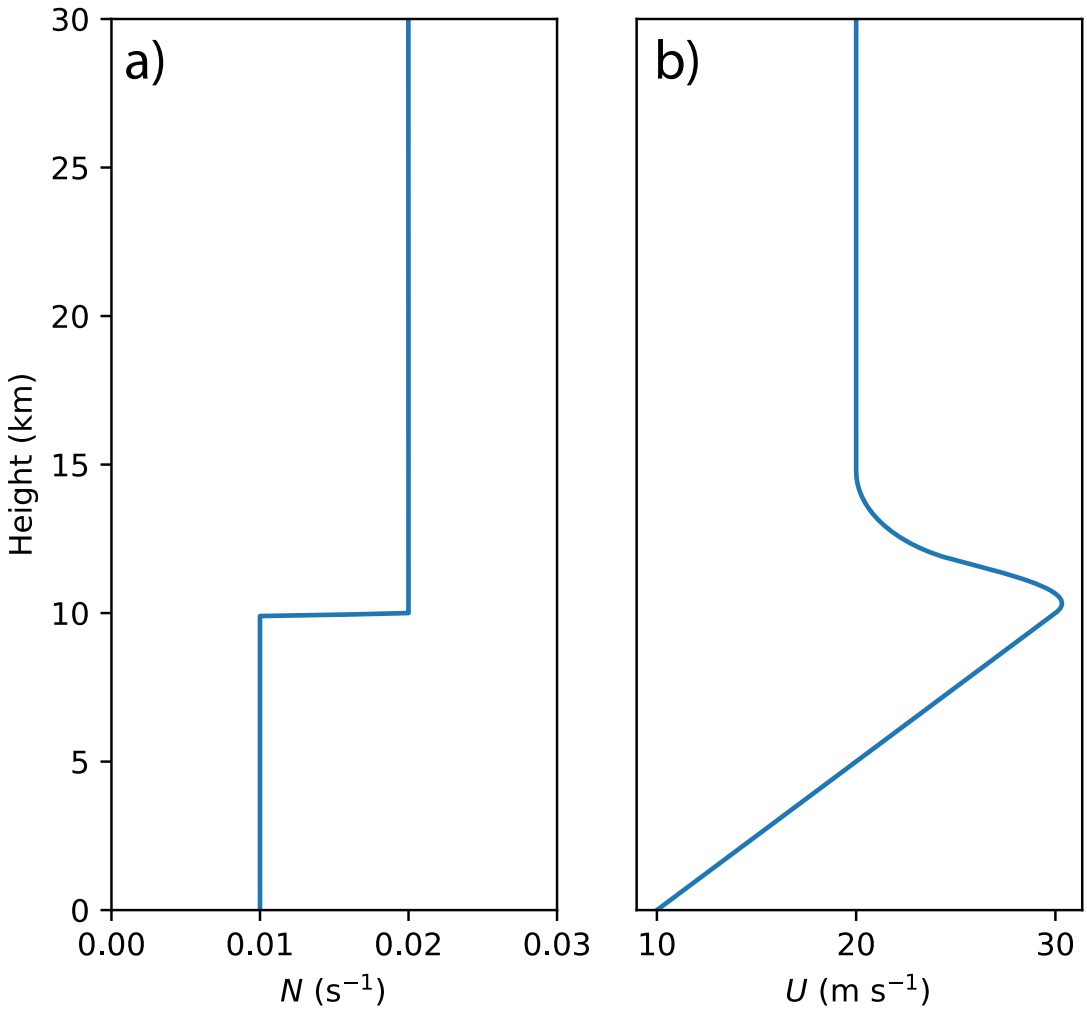

FIGURE 3 Vertical profiles of (a) Brunt-Väisälä frequency N and (b) horizontal wind speed U for an Experiment-3 case with the tropopause height set at 10 km.

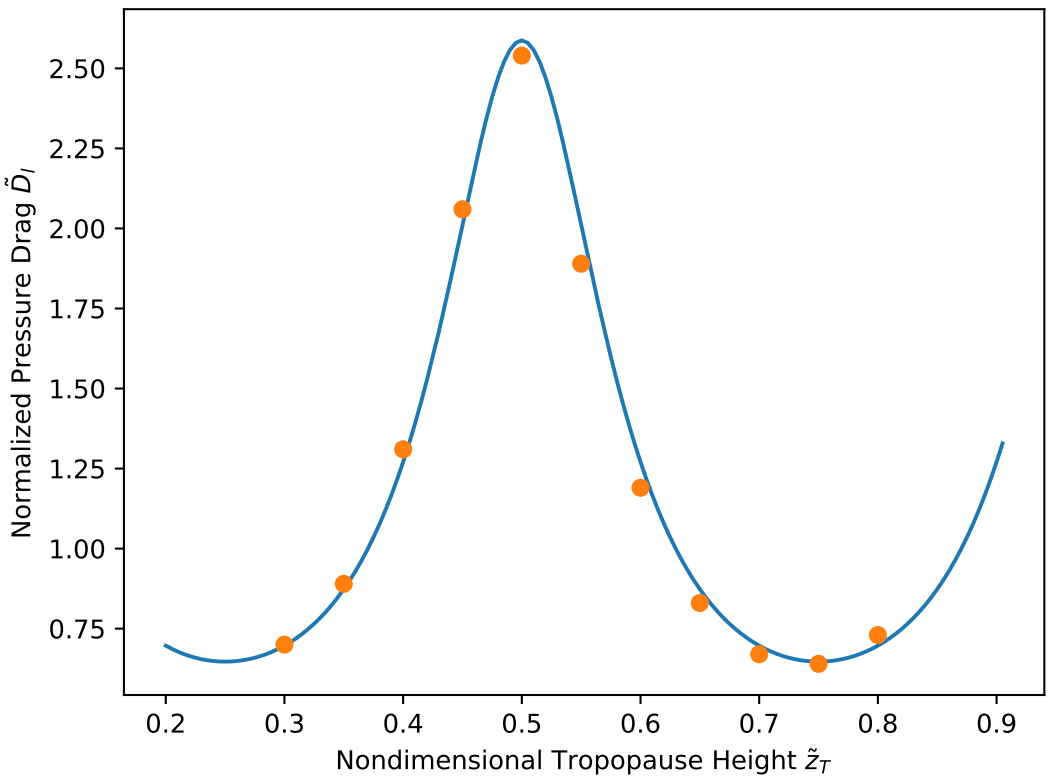

FIGURE 4 Cross-mountain pressure drag $\tilde{D}_l$ as a function of nondimensional tropopause height $\tilde{z}_T$ for Experiment 1 computed by the semi-analytic method (blue line) and using the linearized meso12 model run to steady state (orange points).

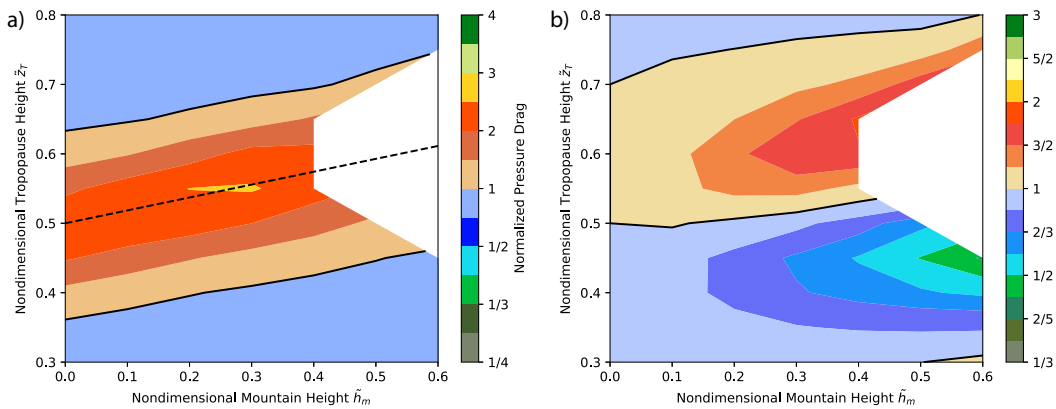

FIGURE 5 (a) Normalized cross-mountain pressure drag $\tilde{D}_{nl}$ for the Experiment-1 simulations contoured as a function of nondimensional mountain and tropopause heights, and (b) Amplification of the nonlinear drag relative to that for the corresponding linear solution. The linear solution is plotted at a mountain height of 0.0. The thick black line indicates a normalized pressure drag or amplification of 1.0. White areas are plotted for those values of $\tilde{h}_m$ and $\tilde{z}_T$ that produce breaking mountain waves. The black dashed line, satisfying $\tilde{z}_T = 1.17\tilde{h}_m + 0.5$, is an empirical fix to the set of $(\tilde{h}_m, \tilde{z}_T)$ along which $\tilde{D}_{nl}$ is maximized and is discussed in connection with Fig. 13.

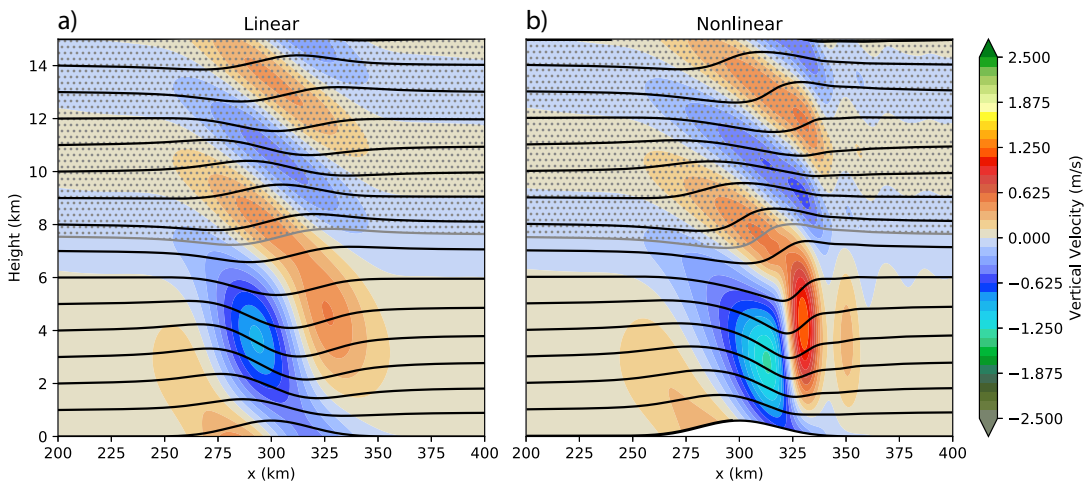

FIGURE 6 Vertical velocity (colour fill) and streamlines (black lines) from the (a) linear and (b) nonlinear meso12 simulations of an Experiment-1 case with nonlinear amplification in which $\tilde{z}_T = 0.55\lambda_L$ and $\tilde{h}_m = 0.3$. The grey line indicates the tropopause, and grey stippling indicates the stratosphere.

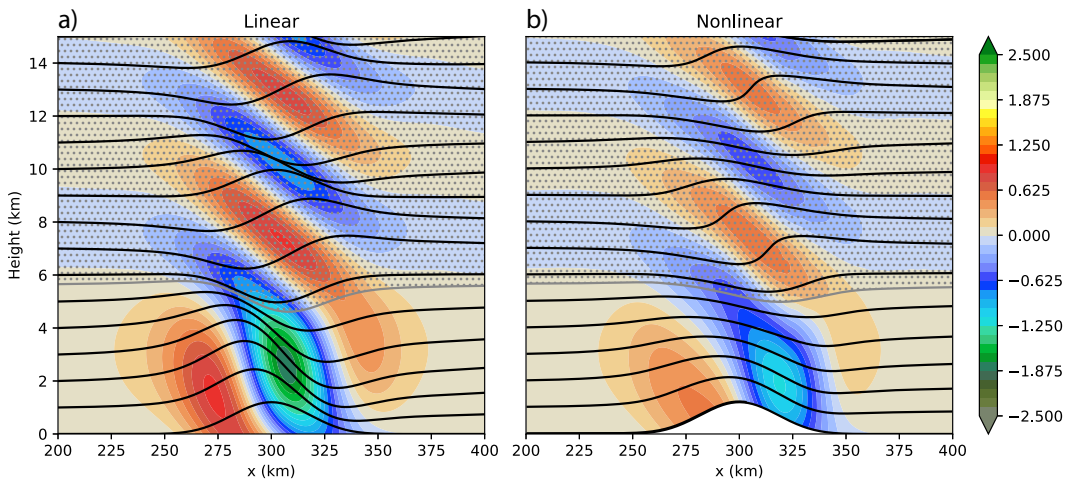

FIGURE 7 As in Fig. 6, but for a case with nonlinear deamplification in which $\tilde{z}_T = 0.45\lambda_L$ and $\tilde{h}_m = 0.6$.

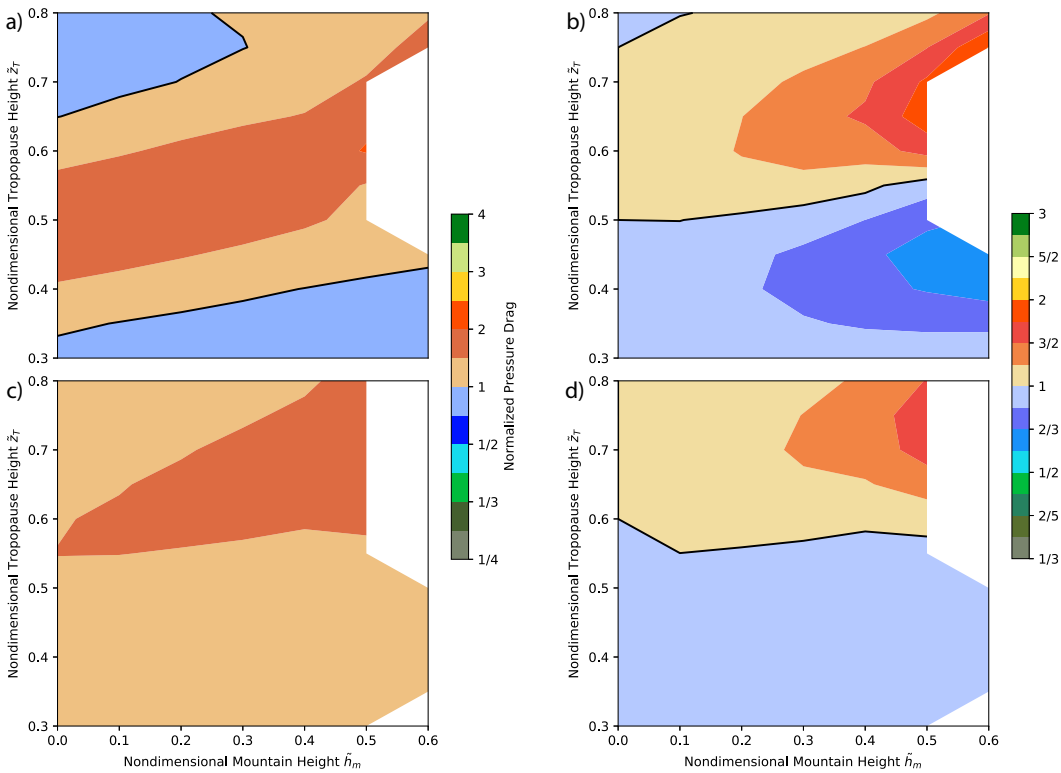

FIGURE 8 Normalized drag $\tilde{D}_{nl}$ as in Fig. 5a for the Experiment-2 simulations with (a) $\Delta z = 1$ km and (c) $\Delta z = 2$ km. Amplification of the drag relative to the linear solution $\tilde{D}_{nl}/\tilde{D}_l$ as in Fig. 5b for cases with (b) $\Delta z = 1$ km and (d) $\Delta z = 2$ km.

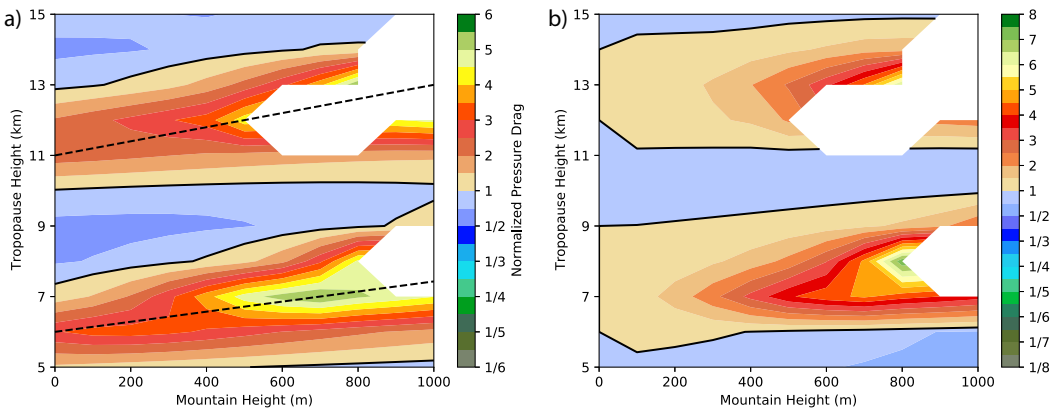

FIGURE 9 (a) Normalized drag $\tilde{D}_{nl}$ and amplification of the drag relative to the linear solution $\tilde{D}_{nl}/\tilde{D}_l$, as in Fig. 5, for the Experiment-3 simulations.

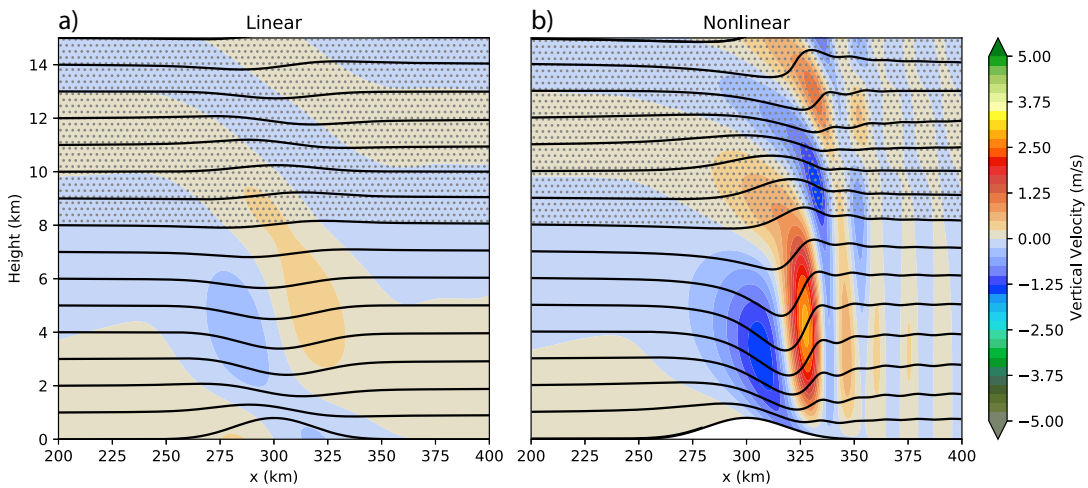

FIGURE 10 As in Fig. 6, but for the 10 m/s to 30 m/s shear sounding with a tropopause height of $z_T = 8$ km and a mountain height of $h_m = 800$ m.

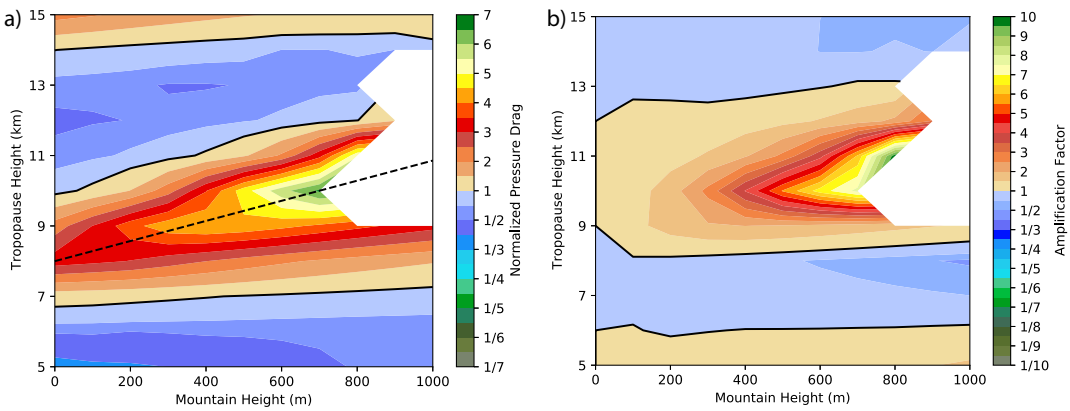

FIGURE 11 (a) Normalized drag $\tilde{D}_{nl}$ and amplification of the drag relative to the linear solution $\tilde{D}_{nl}/\tilde{D}_l$, as in Fig. 5, for the Experiment-3 simulations.

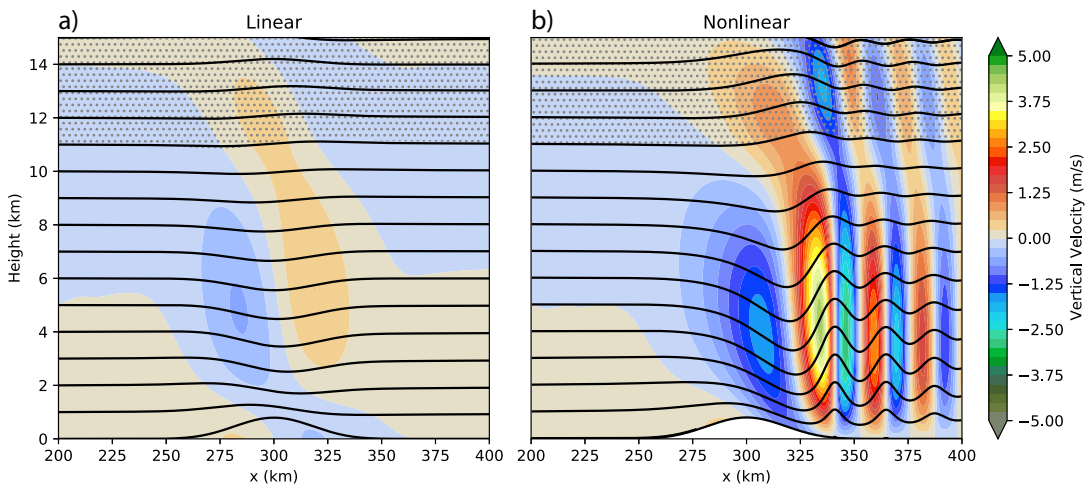

FIGURE 12 As in Fig. 6, but for Experiment 4 with $h_m = 800\,\mathrm{m}$ and $z_T = 11\,\mathrm{km}$.

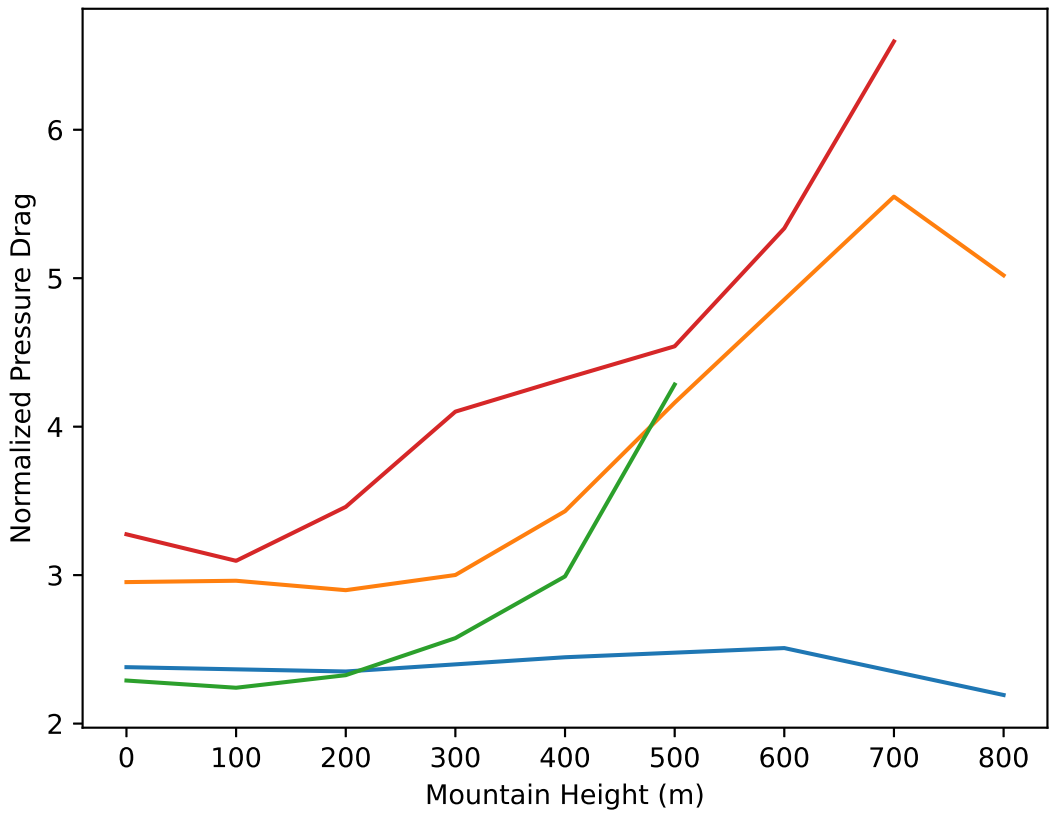

FIGURE 13 Normalized pressure drag as a function of mountain height along the dashed lines in Figs. 5a, 9a and 11a for the no-shear case (blue), the lower-level/upper-level maximum in the 10-30 m/s case (green/orange), and for the 10-50 m/s case (red).

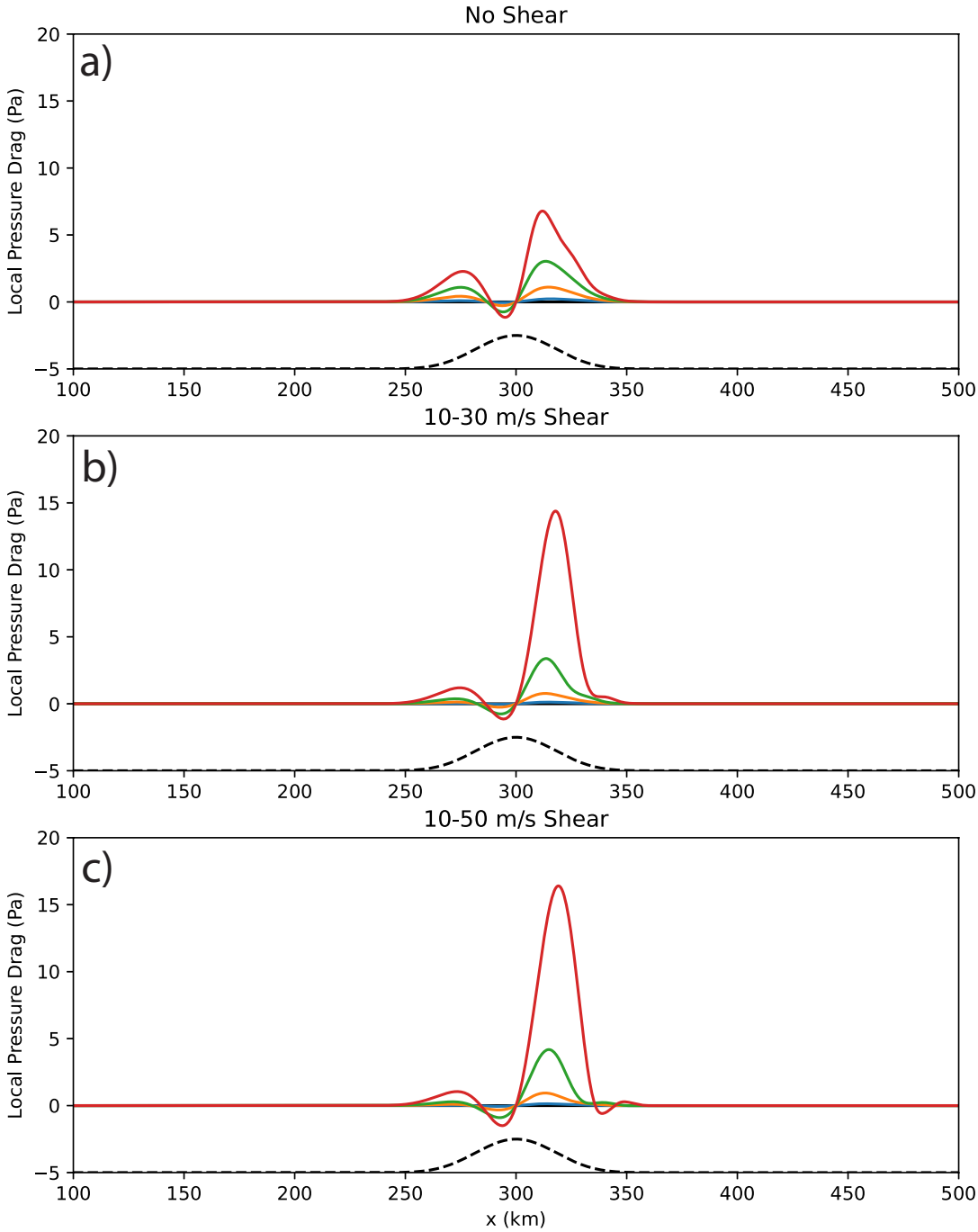

FIGURE 14 Local pressure drag for the (a) no-shear case, (b) 10-30 m/s shear case, and (c) 10-50 m/s shear case. Blue, orange, green, and red lines are for mountain heights of 200 m, 400 m, 600 m, and 800 m, respectively. Tropopause heights are $\tilde{z}_T = 0.65$ for the no-shear case and $z_T = 8$ km and $z_T = 11$ km for the 10-30 m/s and 10-50 m/s shear cases, respectively. For reference, the mountain profile is plotted as a black dashed line.

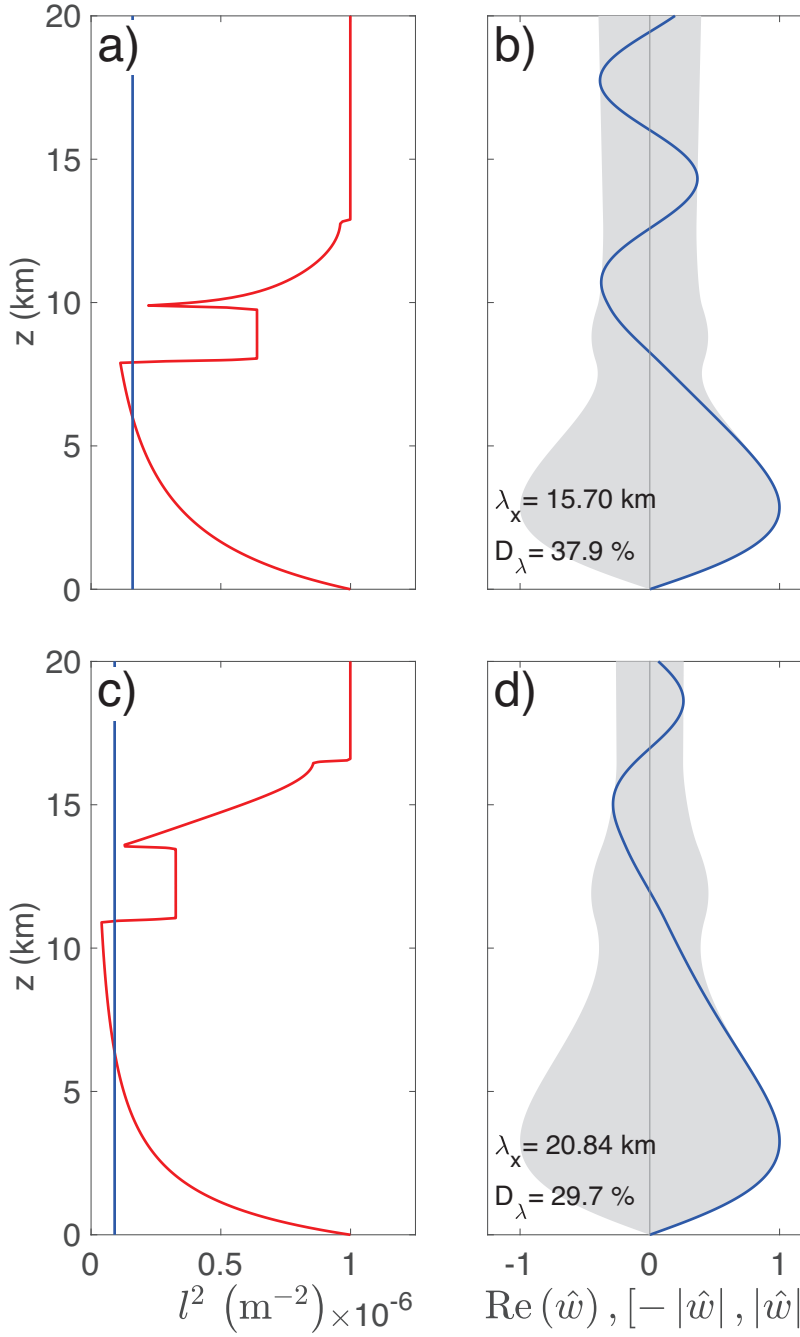

FIGURE 15 Vertical profiles of (a, c) Scorer parameter l squared (red) and (b, d) real part of the Fourier-transformed vertical velocity $\hat{w}(z)$ for the trapped wave mode supported by the (a, b) 10-30 m/s shear case with a tropopause height of 8 km and (c, d) 10-50 m/s shear case with a tropopause height of 11 km. The horizontal wavenumber k of this mode is plotted as the blue vertical line in (a, c). The grey shading in (b, d) indicates the interval $[-\,|\hat{w}|\,,\,|\hat{w}|]$, where $|\hat{w}|$ is the magnitude of $\hat{w}$. The parameters λ_x and D_λ indicate the horizontal wavelength and downstream decay per wavelength, respectively.

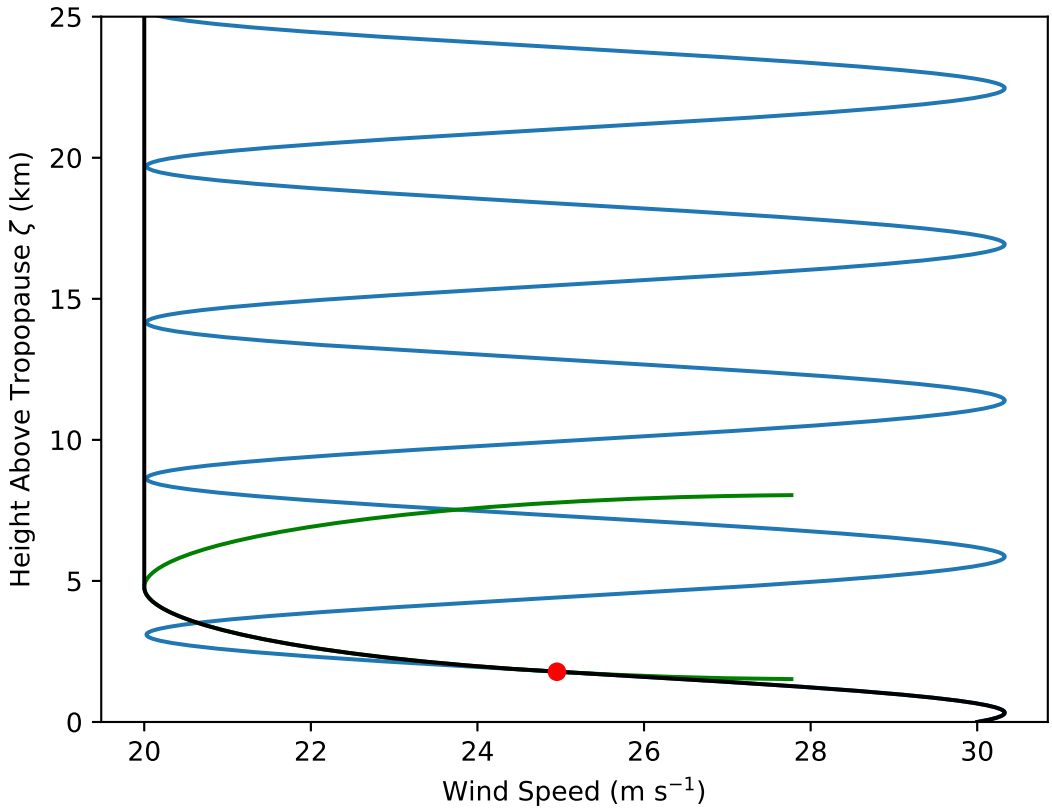

FIGURE 16 Demonstration of the construction of a wind profile in the stratosphere. The blue curve indicates the solution for a constant Scorer parameter l. The red dot indicates the first point with zero curvature above the tropopause, while the green curve indicates the ellipse used to transition between the constant-l and constant-U profiles. The resulting wind profile is shown in black.

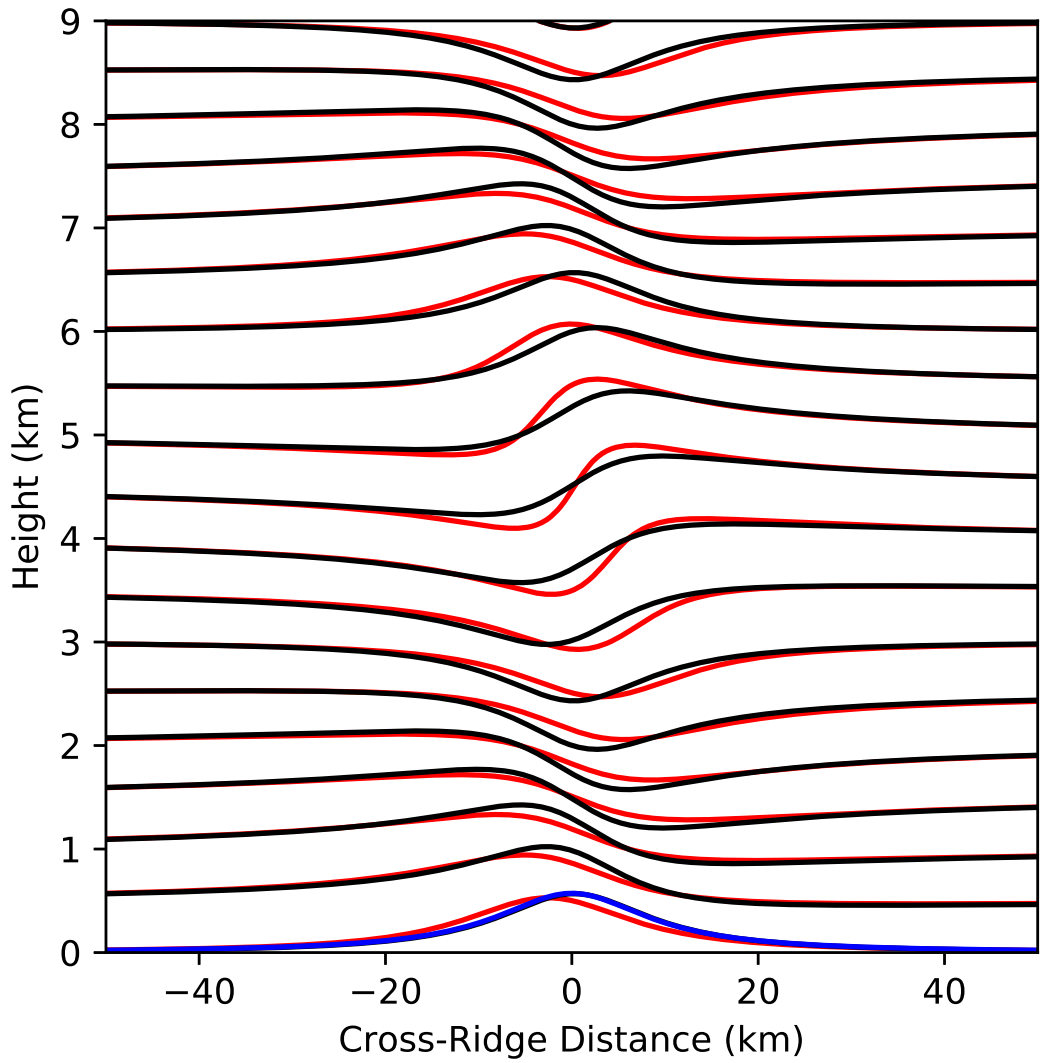

FIGURE 17 Comparison between two methods of plotting linear streamlines in flow from left to right over a Witch of Agnesi mountain: red lines use Eqs. 26 and 27; black lines use Eqs. 28 and 29. The mountain profile is shown in blue and coincides with the lowest black streamline.